DNA transactions and physical environment of chromatin

Ryosuke IMAI

Doctor of Philosophy

Department of Genetics
School of Life Science
SOKENDAI (The Graduate University for Advanced Studies)

DNA transactions and physical environment of chromatin

Imai, Ryosuke

Doctor of Philosophy

Department of Genetics

School of Life Science

SOKENDAI

(Graduate University for Advanced Studies)

2017 (school year)

Contents

List of Figures

Abstract

Our body consists of about 40 trillion cells, each of which contains 2 m of genomic DNA in a nucleus with a diameter of ~10 μm. The long strands of DNA are wrapped around core histone proteins to form nucleosomes and three-dimensionally organized in the cells as chromatin. The chromatin DNA must be read out (RNA transcription) for various cellular functions, and also be copied (DNA replication) for the next cell division while maintaining its integrity (DNA repair). These “DNA transaction” reactions are essential for cell viability. In this thesis, I performed two projects to investigate the interplay between the DNA transaction and chromatin environment using interdisciplinary approaches such as chemical biology, cell biology, biophysics, and computational biology.

At first I report interplay between DNA transaction and chromatin condensation induced by a platinum-based chemical reagent 5-H-Y, which was synthesized by Dr. Seiji Komeda. Platinum-based drugs, such as cisplatin, have been used extensively in cancer chemotherapy. It is well known that the drug–DNA interaction causes covalent DNA crosslinks and subsequent cytotoxicity. I showed that 5-H-Y has a great inhibition ability on human cell growth by arresting the cells in the S/G2 phase, and that 5-H-Y is effective against cisplatin-resistant cancer cells. To understand the cytotoxic mechanism of 5-H-Y, I took an interdisciplinary approach, and revealed that the cytotoxicity is caused by suppression of DNA replication and RNA transcription. Interestingly the cytotoxic mechanism of 5-H-Y is distinct from that of cisplatin: although cisplatin

inhibits cell growth by inducing covalent crosslinks in DNA strands, 5-H-Y has a unique ability to tightly bind to DNA and induce chromatin condensation, instead of crosslinking DNA. Since DNA replication and RNA transcription might occur at opened chromatin at the surface or outside of compact chromatin domains, I propose that 5-H-Y can inhibit the opening of chromatin by condensation and subsequent initiation processes of the DNA transactions in the treated cells. While my study on 5-H-Y will contribute to expanding its clinical applications for cisplatin-insensitive cancers, my study implies that higher order chromatin organization itself is important to proper regulation of DNA transaction reactions for cell survival.

Next, I investigated the chromatin environment in living cells, especially condensed chromatin regions, and its relation to protein accessibility. It is known that chromatin can be roughly categorized into two types, euchromatin and heterochromatin, which correspond to sparse and dense chromatin regions, respectively. Less condensed euchromatin usually contains gene-rich, transcriptionally active regions. In contrast, the dense heterochromatin is gene-poor or transcriptionally silenced. DNA regions located in heterochromatin are generally replicated later in S-phase. Recently various heterochromatin features including heterochromatin-specific proteins and histone modifications were revealed. It seemed to me that the heterochromatin provides a unique opportunity to understand how DNA transaction reactions are regulated in terms of chromatin condensation and its accessibility to proteins.

To look into the interplay between chromatin condensation and protein accessibility, I investigated euchromatin and heterochromatin environments in living cells, from the

viewpoint of density, which can be important for chromatin accessibility of various proteins. For this purpose, I used orientation-independent differential interference contrast (OI-DIC) microscopy, which was developed by Dr. Michael Shribak and is capable of mapping optical path differences, to quantify the density of the total materials of samples. I examined condensed pericentric chromatin in live mouse NIH3T3 cells, a representative heterochromatin model. Although I expected that heterochromatin would be very dense, I found that the total density of heterochromatin (208 mg/ml) was only 1.53-fold higher than that of the surrounding euchromatic regions (136 mg/ml) while the DNA density of heterochromatin was 5.5- to 7.5-fold higher. A similar minor difference was obtained in another classical heterochromatin model, the inactive human X chromosomes of RPE1 cells, which one of the copies of the X chromosome is transcriptionally silenced and condensed. This surprisingly small difference may be due to that non-nucleosomal materials (proteins/RNAs) (~120 mg/ml) are dominant in both chromatin regions. Monte Carlo simulation suggested that non-nucleosomal materials contribute to creating a moderate access barrier to heterochromatin, allowing minimal protein access to regions of DNA transactions.

Finally, from my studies I emphasize the importance of understanding the physical chromatin environments in live cells, which both facilitate and constrain the diffusion of protein factors and their complexes and govern DNA transaction reactions.

Key words: Platinum-based drug, 5-H-Y, cisplatin, cisplatin-resistant cancer cells, DNA replication, FANC/BRCA pathway, DNA crosslink, live cell imaging, differential interference contrast (DIC) microscopy, euchromatin, heterochromatin, inactive X chromosome, density, chromatin organization, access barrier, macromolecular crowding

Chapter 1

Chromatin condensation and DNA replication inhibition mediated by a highly antitumor-active tetrazolato-bridged dinuclear platinum(II) complex

1.1. Introduction

Our body consists of about 40 trillion cells, each of which contains 2 m of genomic DNA in a nucleus with a diameter of ~10 μm. The long strands of genomic DNA are wrapped around histone proteins and organized in cells as chromatin (Watson et al, 2013). This chromatin DNA must be read out (RNA transcription) for various cellular functions, and copied (DNA replication) for the next cell division while maintaining integrity (DNA repair / recombination) (Watson et al, 2013). DNA transactions such as DNA replication/ repair/ recombination and RNA transcription are essential for cell viability and are targets of many anticancer agents currently used in cancer chemotherapy (Davey & Davey, 2008).

Among many anticancer agents, platinum-based drugs are the most commonly used anticancer agents, especially for the treatment of testicular, ovarian, and colorectal cancers. *Cis*-diamminedichloroplatinum (II) (cisplatin, Figure 1) (Kociba et al, 1970; Rosenberg & VanCamp, 1970) is a platinum-based DNA crosslinking agent that first

proved the importance of platinum-DNA interactions (Mansy et al, 1973). Cisplatin and the other platinum-based drugs, such as carboplatin and oxaliplatin (Deans & West, 2011), are considered to work in a similar fashion (Jamieson & Lippard, 1999). The platinum–DNA interactions make both inter- and intra-strand crosslinks in DNA, suppressing DNA replication (Jamieson & Lippard, 1999) and also RNA transcription (Todd & Lippard, 2009). For DNA replication process, intra-strand DNA crosslinks can be bypassed by some translesion (TLS) polymerases (Jamieson & Lippard, 1999). To deal with inter-strand DNA crosslinks (ICLs), mammalian cells have evolved the Fanconi anemia (FA)/BRCA pathway, which is coupled with DNA replication (Kim & D'Andrea, 2012). FA is a rare genetic disorder characterized by progressive bone marrow failure and a highly elevated risk of hematological and squamous cancers (Fanconi, 1967). To date, many FANC genes (more than 25) have been identified from FA patients, whose cells are highly sensitive to ICL-inducing agents, including cisplatin. Although the precise mechanism of ICL repair by the FA/BRCA pathway has not yet been fully understood, it is clear that complex actions of FA proteins, nucleases, TLS polymerases, and homologous recombination proteins are involved. Importantly, loss of any protein involved in the FA/BRCA pathway ultimately leads to hypersensitivity to cisplatin.

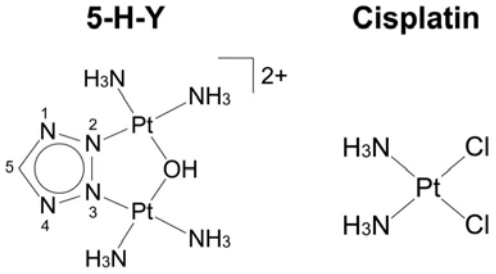

Figure 1. Chemical structures of [{*cis*-Pt(NH_3)$_2$}$_2$(μ-OH)(μ-tetrazolato-*N2*,*N3*)]$^{2+}$ (5-H-Y) (left) and *cis*-diamminedichloroplatinum(II) (cisplatin) (right).

A common problem with cisplatin and its derivatives is that prolonged treatment generates resistant cancer cells (e.g., (Sakai et al, 2008)). Thus, it is important to develop new drugs that can kill cisplatin-resistant cancer cells. However, conventional platinum-based drugs usually have similar anticancer spectra and the clinical platinum-based drugs show cross-resistance (Rixe et al, 1996; Stordal et al, 2007). Thus, a significant structural modification appears to be required to design candidate next-generation, platinum-based drugs (Komeda, 2011; Malina et al, 2011; Park et al, 2012; Peterson et al, 2015; Pickard et al, 2014).

Dr. Seiji Komeda's group previously introduced a series of cationic azolato-bridged dinuclear platinum(II) complexes $[\{cis\text{-}Pt(NH_3)_2\}_2(\mu\text{-}OH)(\mu\text{-azolato})]^{2+}$ (azolato-bridged complexes), which have different structures from the conventional platinum-based drugs and overcome cross-resistance to cisplatin (Komeda et al, 2011; Komeda et al, 2000; Komeda et al, 2013). The azolato-bridged complexes possess a +2 ionic charge (e.g. Figure 1) and are known to interact with DNA both covalently and non-covalently. The covalent interaction provides bifunctional DNA adducts, such as 1,2-intrastrand crosslink with a minimal kink in the DNA (Magistrato et al, 2006; Mlcouskova et al, 2012b; Teletchea et al, 2006), which seems to be difficult to be repaired (Mlcouskova et al, 2012a). Via non-covalent interactions, the azolato-bridged complexes induce a conformational change in DNA structure (Yoshikawa et al, 2011), presumably because of their cationic feature and slow rate of formation of covalent DNA crosslinks (Uemura et al, 2015; Uemura et al, 2012).

The anticancer spectra of these azolato-bridged complexes, based on a panel of 39 human cancer cell lines (JFCR39), differed markedly from those of the conventional platinum-based drugs (Komeda et al, 2013). Thus, their mechanisms of action are also likely to differ. Among the azolato-bridged complexes, [{*cis*-Pt(NH_3)$_2$}$_2$(μ-OH)(μ-tetrazolato-*N2*,*N3*)]$^{2+}$ (5-H-Y) is the most promising anticancer drug candidate (Figure 1), and exhibits strikingly high *in vivo* antitumor efficacy against xenografted pancreatic cancer in nude mice, inhibiting tumor growth by 99% versus untreated controls (Komeda et al, 2011).

In this study, using combined techniques of cell biology, structural biology, and biophysics, I investigated the cytotoxic mechanism of 5-H-Y. I found that the compound inhibits DNA replication and RNA transcription, and arrests treated cells in the S/G2 phase, causing great cytotoxicity. 5-H-Y has much less DNA crosslinking ability than cisplatin, and binds to DNA very tightly, inducing chromatin condensation. I also found that DNA damage by 5-H-Y is repaired differently from ICL generated by cisplatin, and 5-H-Y is effective for cisplatin-resistant cancer cells. This study provides a mechanistic insight into the cytotoxicity of 5-H-Y and also suggests interplay between DNA transaction and chromatin condensation induced by 5-H-Y.

1.2. Results

The novel platinum complex 5-H-Y inhibits cell proliferation

To evaluate the effects of 5-H-Y and cisplatin on cell growth inhibition, I first performed cell proliferation assays using four human cell lines (PC9, HeLa, U2OS, and TIG-1) (Figure 2). PC9, HeLa, and U2OS cells are cancer cell lines and TIG-1 is a 'normal' human fibroblast line. Cell numbers were examined over time under various concentrations of 5-H-Y and cisplatin, from 0 to 96 h. Both drugs inhibited the growth of all cell lines tested in a similar manner (Figure 2), consistent with a previous report (Komeda et al, 2013). These results suggest that 5-H-Y and cisplatin show comparable inhibitory effects on the proliferation of these cell lines.

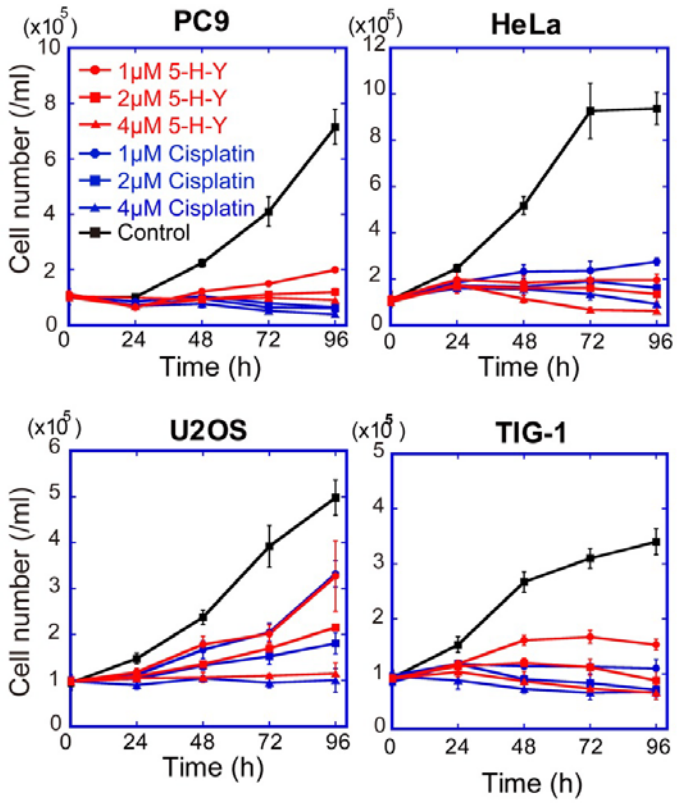

Figure 2. Cell proliferation assays with 5-H-Y or cisplatin treatment.
Four human cell lines (PC9, HeLa, U2OS, and TIG-1) were treated with the indicated concentrations of 5-H-Y or cisplatin, and the cell numbers were monitored from 0 to 96 h for human cells.

5-H-Y is incorporated into cell nuclei

To gain clues into the mechanism of 5-H-Y cytotoxicity, the intracellular localization of 5-H-Y and cisplatin should be investigated. It is normally not possible to examine drug localization by conventional cell biological methods. For this purpose, scanning X-ray fluorescence microscopy (SXFM) (Matsuyama et al, 2010; Shimura et al, 2005) was used as collaboration with Prof. Kazuto Yamauchi at Osaka Univ. and Dr. Mari Shimura at National Center for Global Health and Medicine (NCGM) (Figure 3). This method enables the detection of the target elements at a single-cell level and gives a cellular localization profile of these elements. We examined various element localizations in both 5-H-Y- and cisplatin-treated PC9 cells. Many elements, including phosphorus, sulfur, zinc, and platinum were detected by this SXFM (Figure 4). Signals of phosphorus, sulfur, and zinc mainly reflect on localizations of nucleic acids, proteins, and DNA-binding proteins, respectively (Matsuyama et al, 2010; Shimura et al, 2005). In 5-H-Y-treated cells, platinum was observed throughout the cells, including in the nuclei. The cisplatin-treated cells also showed platinum signals, consistent with previous studies (Matsuyama et al, 2010; Shimura et al, 2005; Takata et al, 2013).

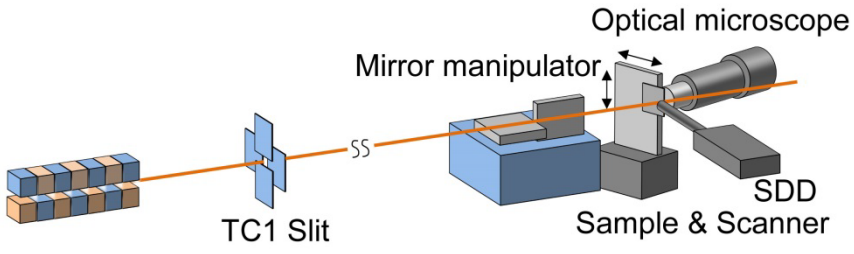

Figure 3. Schematic view of scanning X-ray fluorescence microscopy.
The X-ray beam, highly focused by a set of mirrors (KB-mirror) was focused on the cells. Then X-ray fluorescence was detected by the silicon drift detector (SDD).

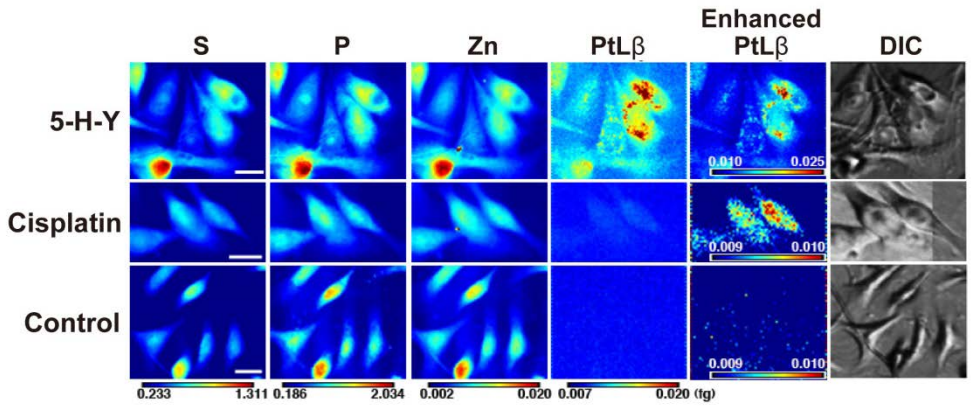

Figure 4. SXFM analysis after drug treatment.

Cell morphologies obtained by Nomarski (DIC). Brighter colors indicate a higher signal intensity of each element. Representative results are shown. Results are shown for 5-H-Y (top) and cisplatin (middle), untreated control PC9 cells (bottom). Note the high intensity of Pt in 5-H-Y treated cells. Pt, platinum signal, P, phosphorus, S, sulfur, Zn, zinc. Color bars indicate elemental content, expressed in fg/μm^2. The phosphorus- and zinc -rich regions in the cells seem to be nuclei. Bars show 10 μm.

To further confirm these findings, I fractionated the drug-treated PC9 cells as whole cells, nuclei (detergent-treated), and naked DNA fractions. The amount of platinum in each was analyzed by inductively coupled plasma-mass spectrometry (ICP-MS). Considerable amounts of platinum were present in all fractions from both cell groups (Figure 5), suggesting that 5-H-Y and cisplatin are incorporated into nuclei and some of the drug interacts tightly with DNA. Because 5-H-Y was detected in nuclei and found even in the DNA fraction, similar to the case of cisplatin, I next paid attention to DNA replication and RNA transcription.

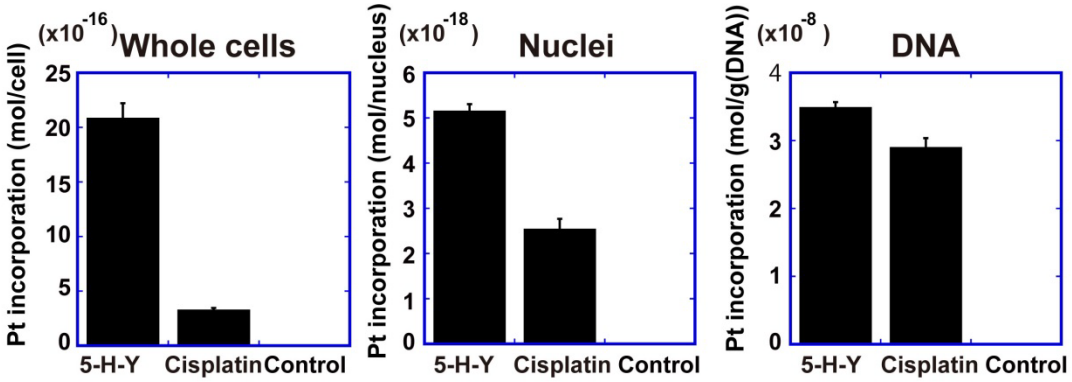

Figure 5. Amounts of platinum in PC9 whole cells, nuclei, and DNA fractions of 5-H-Y- and cisplatin-treated cells.

5-H-Y inhibits DNA replication and arrests the cell cycle in the S/G2 phase

Cisplatin binds covalently to DNA, which trigger inhibition of DNA replication, causing cell cycle arrest in the S/G2 phase (Fujikane et al, 1989). To examine the effects of 5-H-Y on the cell cycle, I monitored the cell cycle stages of drug-treated (24 h) HeLa, U2OS, PC9, and TIG-1 cells, using flow cytometry (FCM) (Figures 6, 7, and 8). Cisplatin inhibited the incorporation of a thymidine analog, 5-ethynyl-2'-deoxyuridine (EdU), into newly synthesized DNA, suggesting that DNA replication was inhibited (Figures 6 and 7). Consistently, cisplatin-treated cells were arrested in the S/G2 phase (Figure 6). In 5-H-Y-treated cells, a 3- to 10-fold reduction of EdU incorporation and cell cycle arrest in S/G2 were observed, similar to the effects of cisplatin (Figure 6). Furthermore, I synchronized HeLa cells at the G1/S phase boundary before treatment with 5-H-Y for 15 h (Experimental scheme is shown in Figure 9). EdU incorporation was almost completely inhibited after release from the G1/S block (Figure8). These results suggest that 5-H-Y has an inhibitory effect on DNA replication, as does cisplatin.

While I observed a similar inhibition of DNA replication between the cells treated with

5-H-Y and cisplatin for 15 h (Figure 8) or 24 h (Figures 6 and 7), I found that 5-H-Y has a more rapid effect on DNA replication than cisplatin (Figure 10). When HeLa cells were treated with the drugs for 2 h, 5-H-Y inhibited DNA replication more severely than cisplatin (Figure 10). This effect was also observed in other human cell lines (Figure 10B).

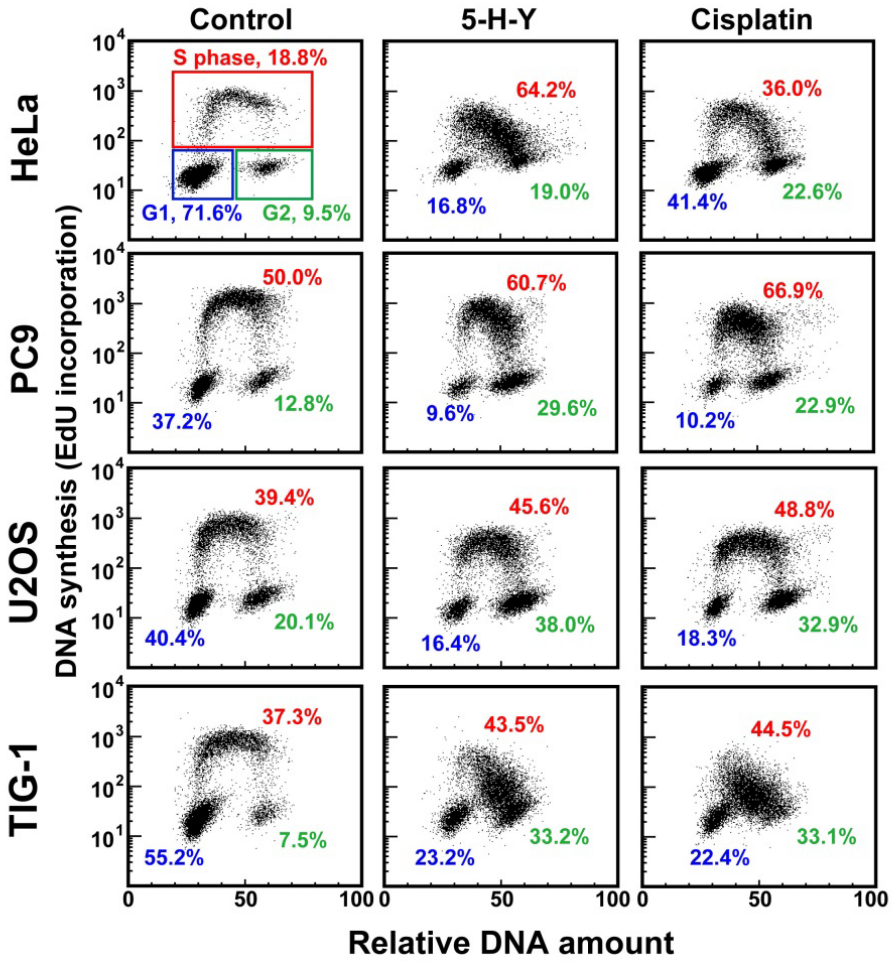

Figure 6. Flow cytometry results for HeLa (1st row), PC9 (2nd row), U2OS (3rd row), and TIG-1 cells (4th row) with/without 2 μM of 5-H-Y or cisplatin.
Vertical and horizontal axes show DNA synthesis activity (EdU incorporation) and DNA amount, respectively. Each dot represents a single cell and results using 10,000 cells are plotted. In the plot of control HeLa, the corresponding cell cycle stages are indicated. Percentages of each cell cycle population are indicated.

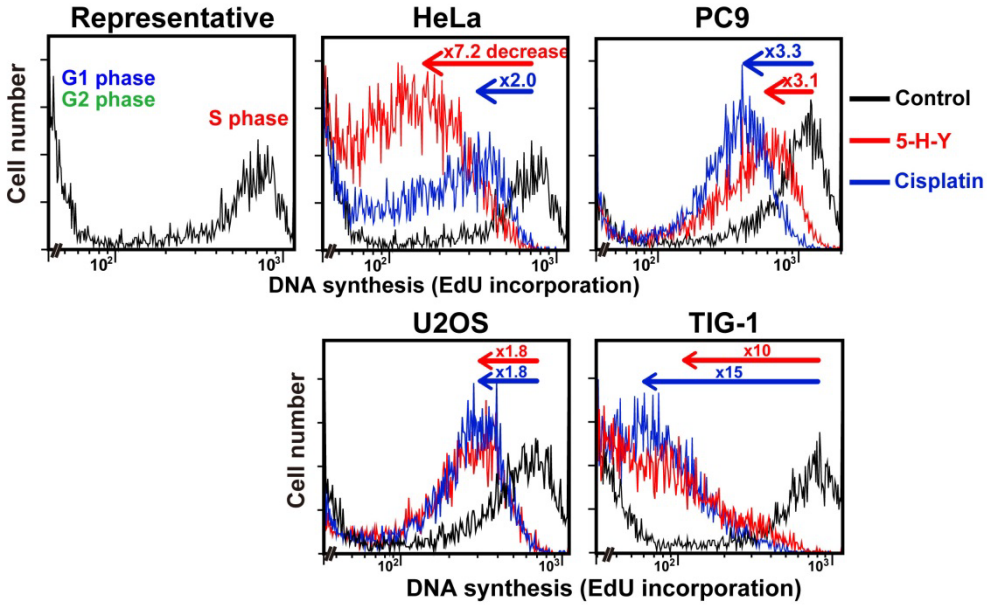

Figure 7. EdU incorporation versus cell numbers plots of Figure 6.

Upper left panel shows a representative plot (control HeLa). Note that EdU incorporation was high in the S-phase. Fold decreases in EdU incorporation upon 5-H-Y (red) or cisplatin (blue) treatment are indicated in the plots of HeLa (upper middle), PC9 (upper right), U2OS (lower middle), and TIG-1 (lower right). Note the several-fold decreases in EdU incorporation in the 5-H-Y (red) or cisplatin (blue) treated cells.

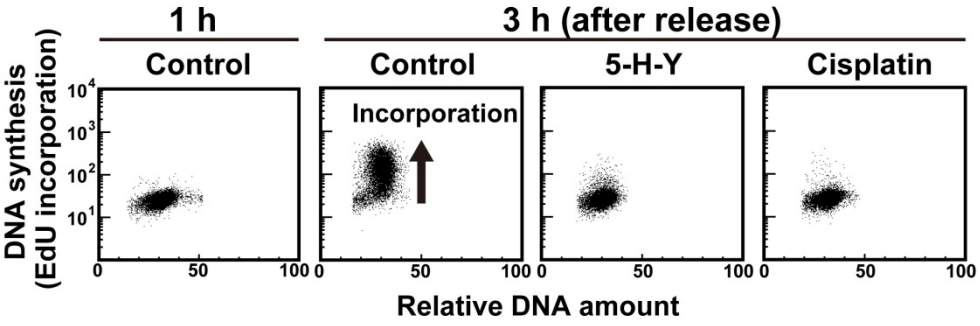

Figure 8. Results for HeLa cells synchronized at G1/S by nocodazole-thymidine block with/without 2 μM of 5-H-Y or cisplatin.

5-H-Y and cisplatin both shows inhibition of very early phases of DNA replication.

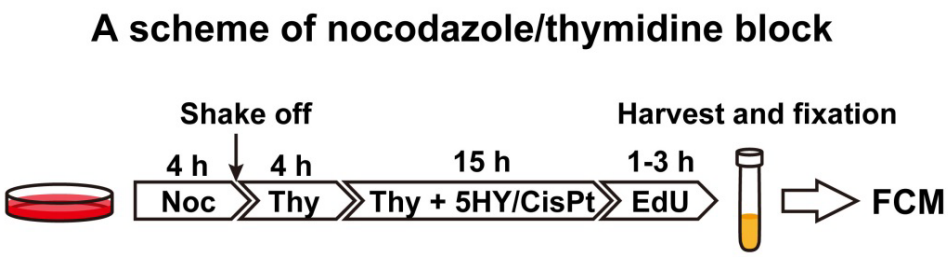

Figure 9. Schematic of nocodazole-thymidine block to collect G1/S cells.

Unsynchronized HeLa cells were treated with 80 ng/mL nocodazole for 4 h. After synchronization at the mitotic phase, mitotic cells were isolated by shaking off and were incubated in medium containing 2.5 mM thymidine to block the cells in the G1/S phase. Then, 4 h later, 2 μM 5-H-Y or cisplatin was added to thymidine-containing medium and the cells were incubated for a further 15 h. Then the synchronized cells were released from the thymidine block and labeled with 10 μM EdU for 1or 3 h. Harvesting and staining for FCM were the same as for unsynchronized cells.

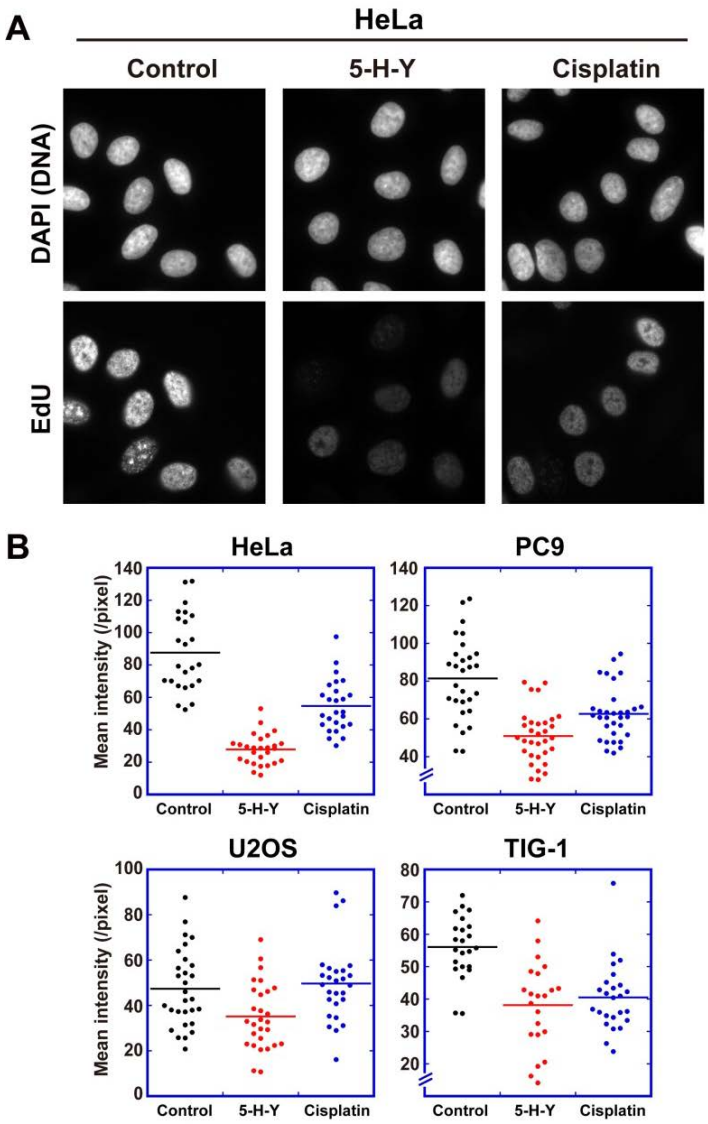

Figure 10. Effect of short-time treatment of 5-H-Y on DNA replication in the four human cell lines. (A) DNA replication foci in HeLa cell nuclei were labeled with EdU and observed by fluorescent microscope. In a short time, 5-H-Y is more effective to inhibit DNA replication than cisplatin. (B) Average intensities in each cell were quantified and plotted (lower) (each group, N >20).

5-H-Y reduces RNA transcription.

Since it was reported that cisplatin could inhibit RNA transcription e.g. (Todd & Lippard, 2009), I examined effect of 5-H-Y on RNA transcription by incorporation of 5-Ethynyl uridine (EU). 5-H-Y treatment decreased the EU incorporation into newly

synthesized RNA in the cells (Figure 11), suggesting that global RNA transcription was reduced in the treated cells. Consistent with the previous reports, the EU incorporation in cisplatin-treated cells was also reduced (Figure 11).

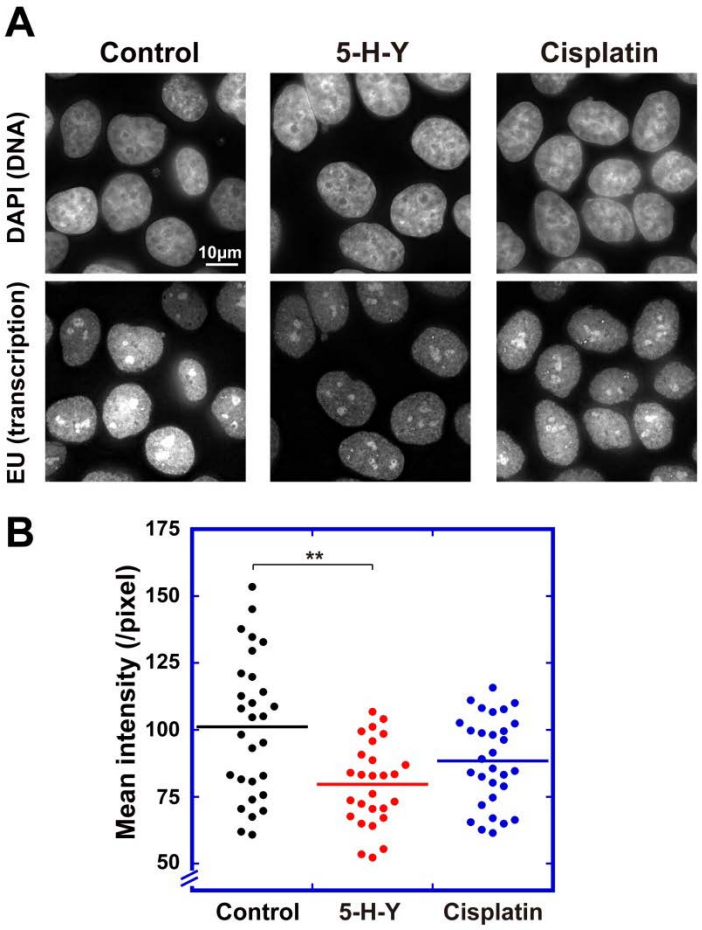

Figure 11. Effect of 5-H-Y on RNA transcription *in vivo*.
(A) Fluorescence microscopy images of 5-H-Y- or cisplatin-treated cells. DNA stain, upper; EU fluorescent labeling, lower. (B) Dot plot of the mean intensity of EU fluorescence in each nucleus (each group, n = 27-30). **p < 0.01, Student's t-test.

5-H-Y induces fewer γH2AX foci than cisplatin

Next, I examined foci formation of phospho-H2AX (γH2AX) in the 5-H-Y-treated cells, which are often associated with DNA double-strand breaks (DSBs)(Mah et al, 2010;

Rogakou et al, 1998) (Figure 12). I observed γH2AX foci in various 5-H-Y-treated cells, such as HeLa, PC9, and TIG-1 cells, but the foci were significantly fewer and weaker than those observed in cisplatin-treated cells (Figures 12 and 13). In addition, in PC9 cells, the γH2AX-foci localization seemed to differ between 5-H-Y- and cisplatin-treated cells: the foci with cisplatin were enriched in the nuclear rim, while those with 5-H-Y were localized more uniformly in the nucleoplasm (Figure 13). Furthermore, when I examined checkpoint activation by hyperphosphorylation of the checkpoint mediator Chk1 in the 5-H-Y treated cells, significantly lower levels of Chk1 phosphorylation were seen than in cisplatin- or mitomycin C-treated cells (Figure 14). These results suggest that DNA damages induced by 5-H-Y are somehow distinct from those by cisplatin.

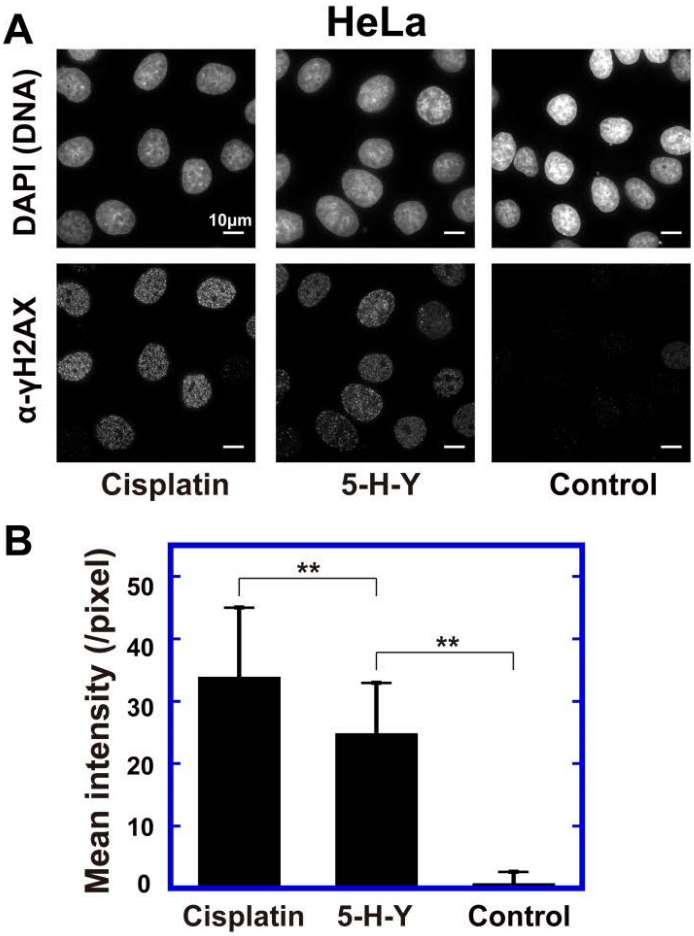

Figure 12. γH2AX foci formation in 5-H-Y- or cisplatin-treated HeLa cells.
(A) DNA stain, upper; anti-γH2AX antibody staining, lower. Scale bars are 10 μm. (B) Quantification of the γH2AX signal intensity averaged from ~50 nuclei. Note that the signal in 5-H-Y-treated cells was significantly lower than in cisplatin-treated cells. **$p < 0.01$, Student's t-test.

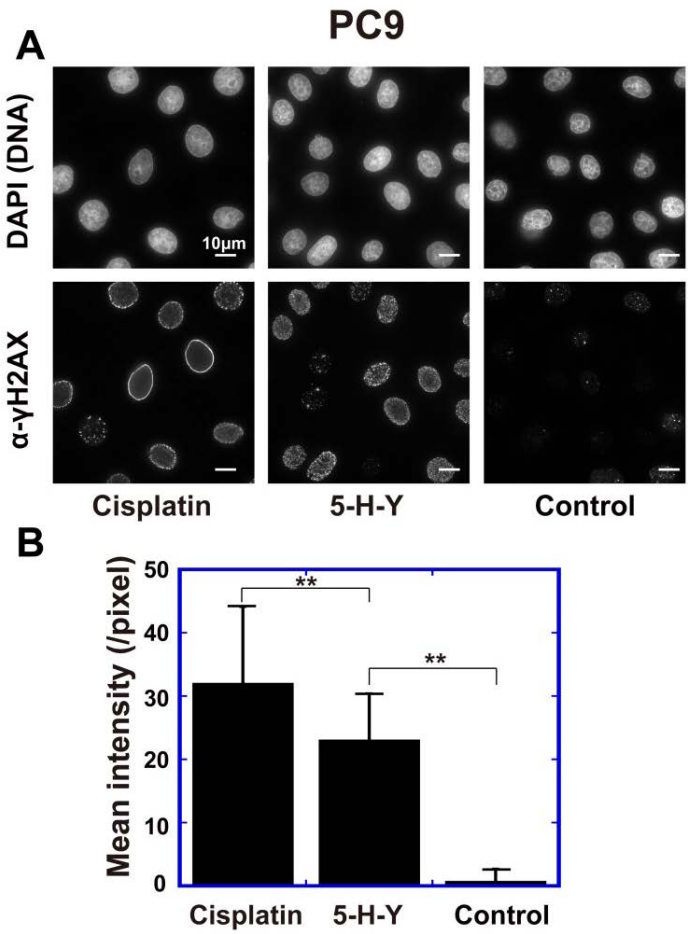

Figure 13. γH2AX foci formation in 5-H-Y- or cisplatin-treated PC9 cells.
(A) DNA stain, upper; anti-γH2AX antibody staining, lower. Scale bars show 10 μm. The signal in 5-H-Y-treated cells was localized mainly in the nuclear periphery, which seemed to be different from the signal localization in cisplatin-treated cells. (B) Quantification of the γH2AX signal intensity averaged from ~50 nuclei. **$p < 0.01$, Student's t-test.

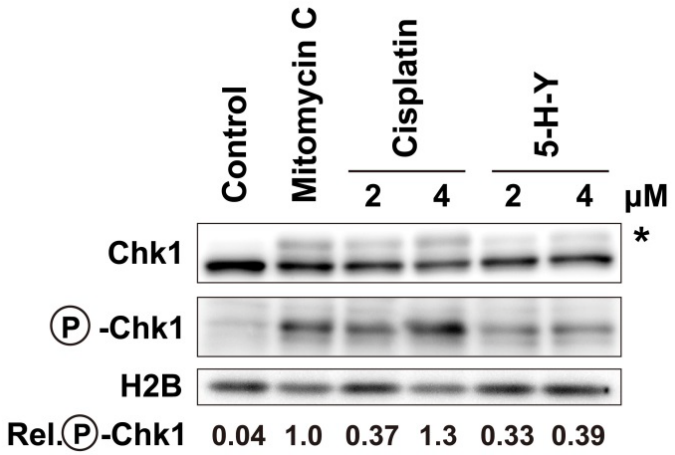

Figure 14. Chk1 activation on drug treatment.

Western blotting analysis of cell lysates using anti-Chk1 (1st row) and anti-phospho-Chk1 (P-Chk1) (2nd row) antibody. In the 1st row, the position of phosphorylated (activated) Chk1 is marked by the asterisk. Control, no treatment; mitomycin C, mitomycin C treatment for efficient DNA crosslinking. The third row is a loading control using H2B. The values at the bottom indicate quantification of the phosphorylated Chk1 signal intensity. Note that the relative intensity of phosphorylated signal in 5-H-Y-treated cells was considerably lower than that in cisplatin-treated cells. The blots were cropped at the positions of the proteins for clarity and space considerations.

5-H-Y provides less amount of DNA crosslinks.

To investigate the DNA crosslinking ability of 5-H-Y, DNA purified from calf thymus was incubated with 5-H-Y or cisplatin for various periods of time. Quantification analysis showed that ~5-fold less 5-H-Y than cisplatin was bound covalently to DNA (Figure 15).

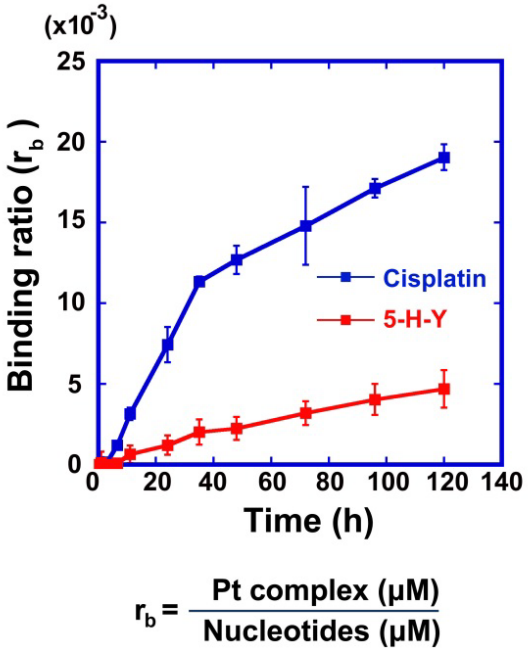

Figure 15. Covalent binding of cisplatin (blue) and 5-H-Y (red) to calf-thymus DNA (*n* = 4). The r_b value is defined as the molar ratio of platinum complex bound per nucleotide.

Next, the frequency of inter-strand DNA crosslink (ICL) formation was directly examined using drug-treated plasmid DNAs (pUC19 and pBluscript) separated in alkaline agarose gel (Figure 16). In both cisplatin-treated plasmid DNAs, there was much more dsDNA (representing ICLs; arrowheads in Figure 16) than in 5-H-Y-treated DNAs, suggesting that 5-H-Y induces 2.2- to 5.9-fold less ICL than cisplatin.

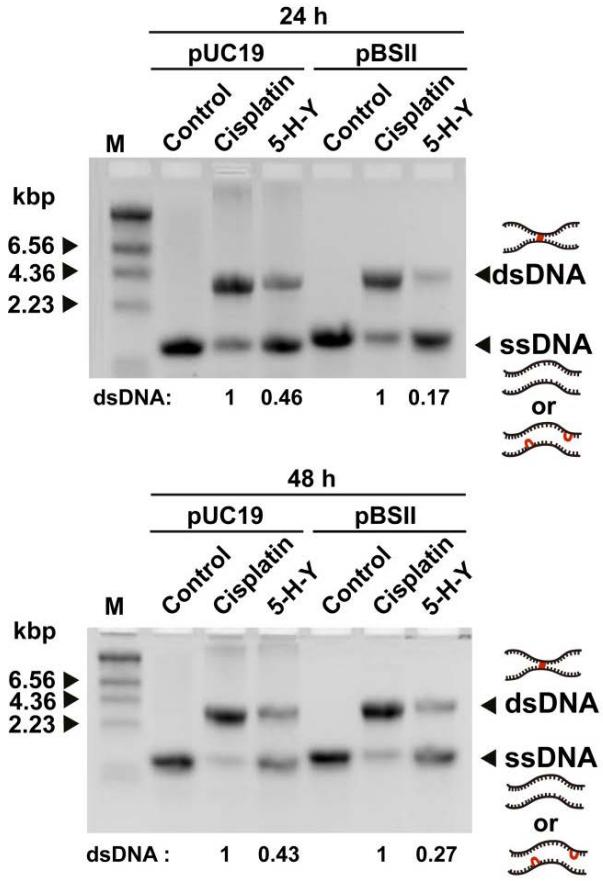

Figure 16. Interstrand crosslinking of drug-treated plasmid DNA.
Two types of plasmid DNAs, pUC19 (left) and pBluescript II (pBSII) (right), were treated with no drug (Control), cisplatin, or 5-H-Y for 24 h (upper) or 48 h (lower). The treated plasmid DNAs were electrophoresed on alkaline agarose gels. The gels with EtBr staining are shown. The positions of dsDNA, representing interstrand crosslinks, and ssDNA, including no crosslinks and intrastrand crosslinks, are shown. Values below the gels indicate intensities of dsDNA normalized by that of cisplatin. Note that there is much more dsDNA in cisplatin-treated DNA than in 5-H-Y-treated DNA. The two DNA templates, pUC19 and pBSII, produced similar results.

Furthermore, we performed semi-quantitative PCR using 5-H-Y- or cisplatin-treated DNAs (pUC19 and pBluescript) as the template (Figure 17). The plasmid DNAs were treated with 5-H-Y- or cisplatin, purified and used as template DNAs for PCR. In the PCR with the cisplatin-treated template, ~10-fold less PCR products were detected than with 5-H-Y-treated one (Brackets in Figure 18 and Figure 19). Because PCR using

mixed DNA templates of cisplatin-treated and untreated plasmids showed successful amplification (the “Cisplatin + Control” lanes in Figure 18), DNA crosslinks, not DNA polymerase inhibition by cisplatin, suppressed the PCR reaction. The two DNA templates, pUC19 and pBluescript, produced similar results and showed no DNA sequence dependency (Figure 18), concluding that 5-H-Y generates intra- and inter-strand crosslinks with much lower frequency compared to cisplatin.

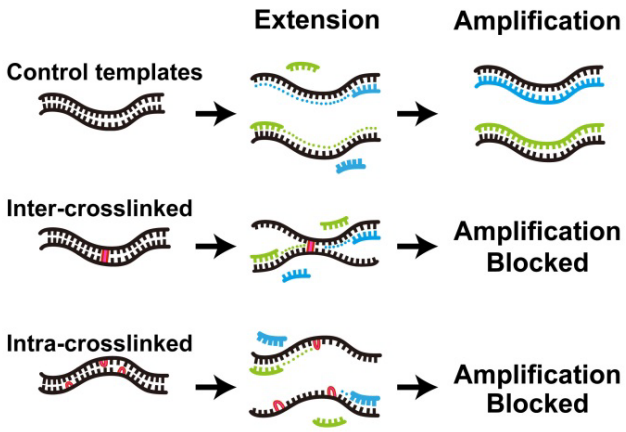

Figure 17. Experimental scheme of PCR amplification.
DNA templates were treated with cisplatin or 5-H-Y. If inter-strand (middle) or intra-strand (bottom) crosslinks occur in the template DNA, DNA amplification by PCR is inhibited.

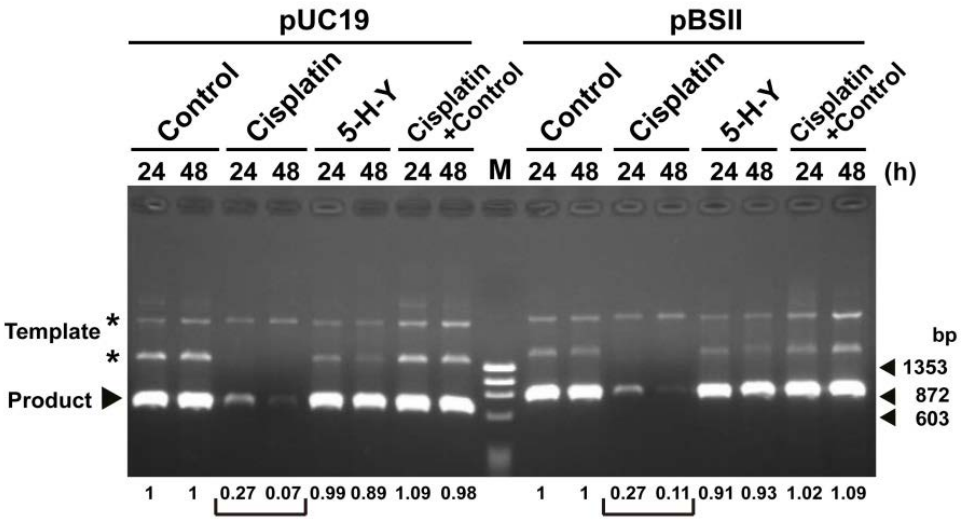

Figure 18. Results of PCR-based crosslinking ability assay.

Two types of plasmid DNAs, pUC19 (left) and pBluescript II (pBSII) (right), were used as PCR templates. They were treated with no drug (Control), cisplatin, or 5-H-Y for 24 h or 48 h. The PCR products (marked with arrow) on the agarose gel after electrophoresis are shown. Bands marked with asterisks are likely to be templates or non-specific amplification. Values below the gel indicate the fluorescent intensities of the PCR product normalized by that of control. In the “Cisplatin+Control” lanes, PCR was performed using mixed templates of cisplatin-treated and no-treated plasmids. Note that PCR using cisplatin-treated template produced much less product.

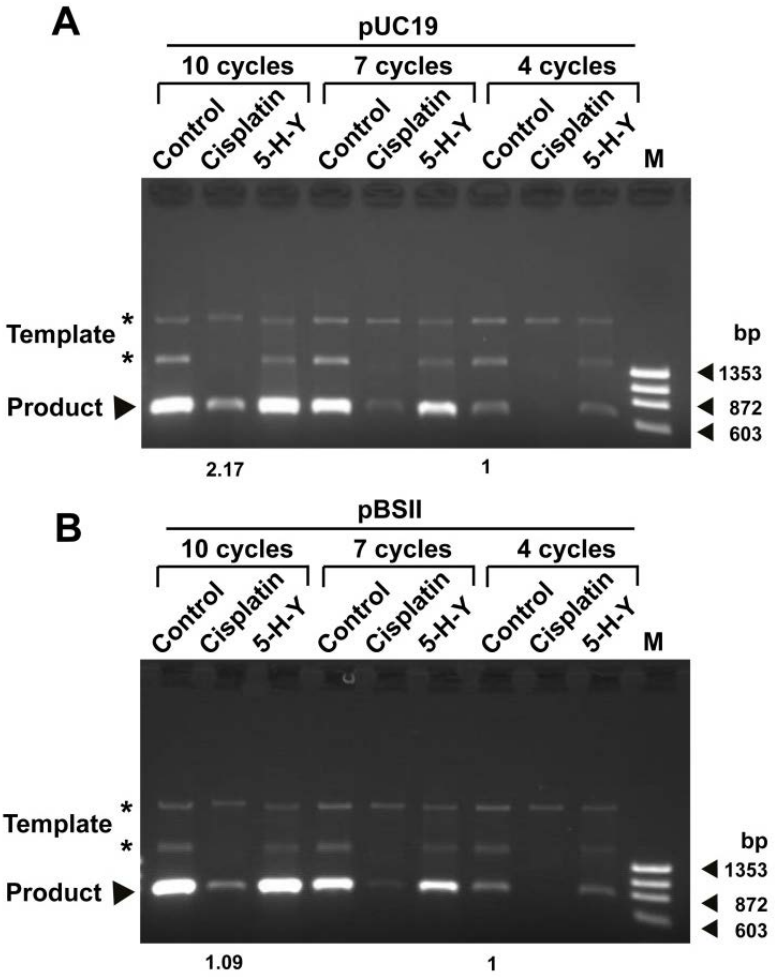

Figure 19. Semi-quantitative PCR with drug-treated templates.
PCR reactions were performed with various cycle numbers (10, 7, or 4 cycles) for no drug (Control), cisplatin-, or 5-H-Y-treated pUC19 (A) or pBluescript II (pBSII) (B). The PCR products (marked with arrow) on the agarose gel after electrophoresis are shown. Bands marked with asterisks are likely to be templates or non-specific amplification. Note that the amount of product for the PCR at 10 cycles using cisplatin-treated template is similar to the control product at 4 cycles.

5-H-Y binds tightly to chromatin DNA and folds chromatin in vitro and in vivo

How does 5-H-Y inhibit DNA replication and RNA transcription? Because 5-H-Y is positively charged and induces compaction of naked DNA(Yoshikawa et al, 2011), the effects of 5-H-Y on higher-order chromatin structure were examined as a collaboration with Prof. Jeffrey C. Hansen at Colorado state Univ. To quantitate chromatin structure in

solution *in vitro*, arrays of 12 positioned nucleosomes were reconstituted from pure histones and DNA as a model chromatin (Figure 20, top), followed by sedimentation velocity experiments in an analytical ultracentrifuge (Figure 20, bottom). The degree of folding of the 12-mer nucleosomal arrays was described quantitatively by the sedimentation coefficient (S) (Hansen, 2002). The extended beads-on-a-string conformation sediments at ~29 S, whereas folding causes the nucleosomal arrays to become compact and increases the sedimentation coefficient to ~40–55 S (Hansen, 2002). When the nucleosomal arrays were exposed to 5-H-Y, the sedimentation coefficient increased, from 27 S to 40–55 S, in a dose-dependent manner. In contrast, cisplatin did not affect the sedimentation of the nucleosomal arrays (Figure 21). These results indicate that 5-H-Y, but not cisplatin, induced condensation of nucleosomal arrays *in vitro*.

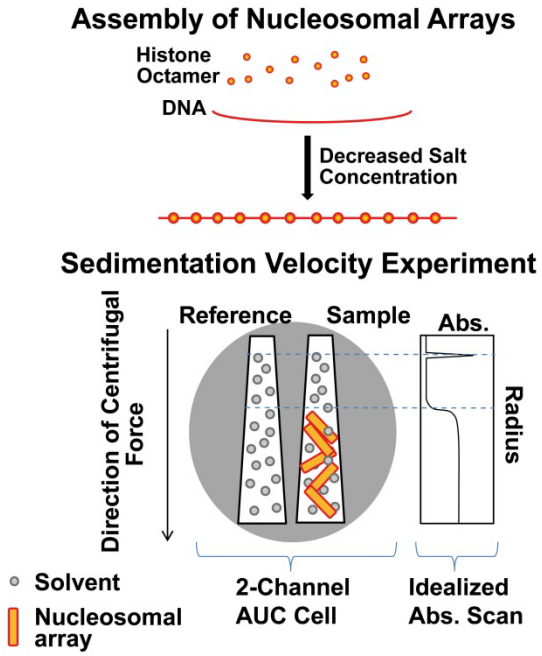

Figure 20. Experimental scheme of the ultracentrifuge assay.

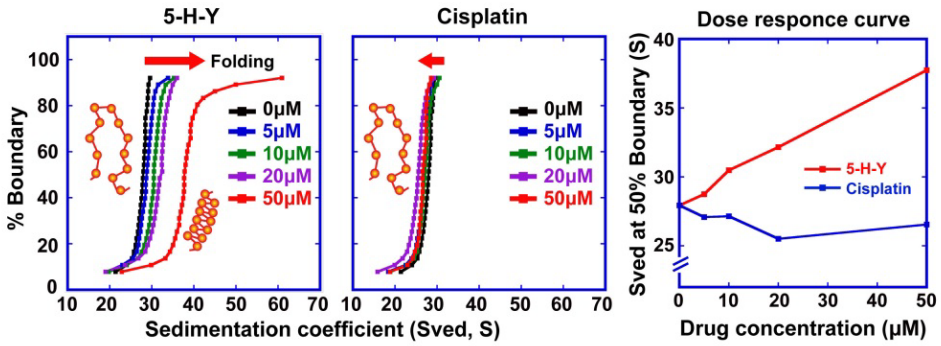

Figure 21. Ultracentrifuge assay showed chromatin folding/condensation activity of 5-H-Y. Samples of reconstituted nucleosome fibers were exposed to the indicated concentrations of 5-H-Y (left) or cisplatin (center) and analyzed by sedimentation velocity analytical ultracentrifugation. The integral distribution of diffusion-corrected sedimentation coefficients obtained after analysis of the data by the method of Demeler and van Holde are shown (Demeler, 2005; Van Holde & Weischet, 1978). (right) Summary of analytical ultracentrifuge-SV results. Values at the 50% boundary are displayed as a function of drug concentration added 5-H-Y (red) or cisplatin (blue).

To further investigate nuclear chromatin condensation by 5-H-Y, volume of permeabilized human cell nuclei attached to glass surfaces was measured (Figure 22) (Takata et al, 2013). Because chromatin is negatively charged, the compaction states of nuclei and their chromatin depend on the cation concentration in the environment (Maeshima et al, 2014; Takata et al, 2013). For example, in low cation environments (e.g., low Mg^{2+} concentration), nuclear chromatin unfolds, leading to an expansion of nuclear volume (Takata et al, 2013). However, nuclear chromatin in the presence of a cation (e.g., 5 mM Mg^{2+}) becomes highly condensed and the nuclear volume decreases (Takata et al, 2013). As shown in Figure 23, nuclear volume, measured with a confocal laser scanning microscope, decreased with the addition of 5-H-Y in a concentration-dependent manner. These results indicate that 5-H-Y can induce the folding of nuclear chromatin. Notably, permeabilized nuclei pre-treated with 5-H-Y did not increase in volume even after washing with low-salt buffer, while nuclei pre-treated

with 5 mM Mg^{2+} unfolded greatly after washing (Figure 24). This suggests that 5-H-Y binding to nuclear chromatin DNA is quite tight and not a simple electrostatic attraction.

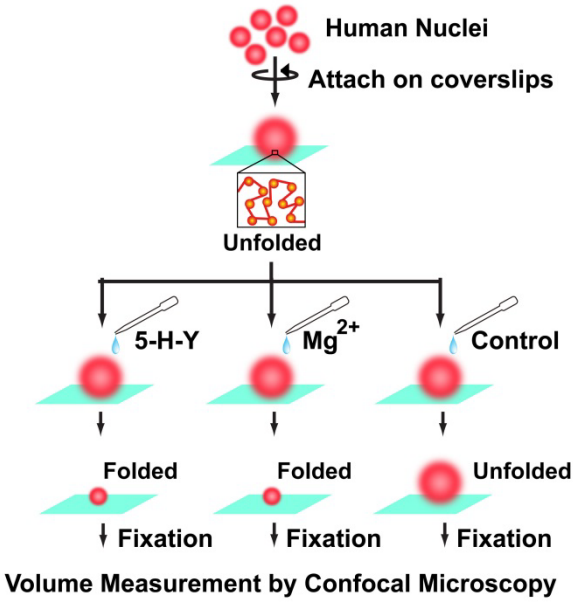

Figure 22. Experimental scheme of the nuclear volume assay.

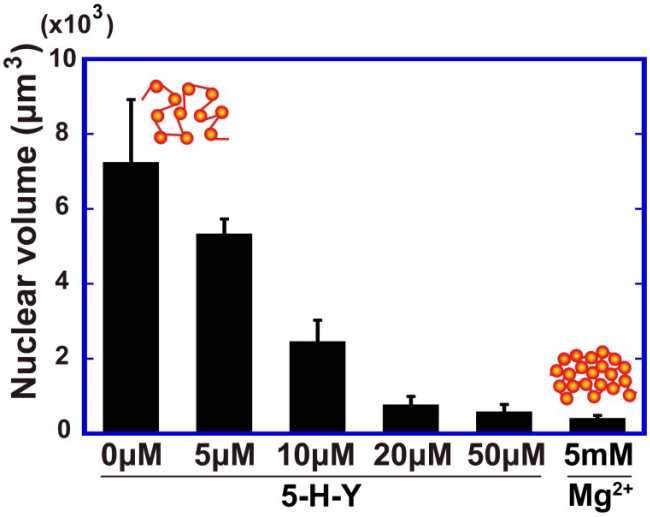

Figure 23. Nuclear volume was decreased by 5-H-Y in a dose-dependent manner.
Nuclei treated with 50 μM 5-H-Y showed a 12-fold decrease in the volume. This indicates that 5-H-Y induces chromatin folding. The nuclei treated with 5 mM Mg^{2+} were prepared as a control for the nuclei with highly folded chromatin. The error bars represent the standard deviation. For each point, n = ~100.

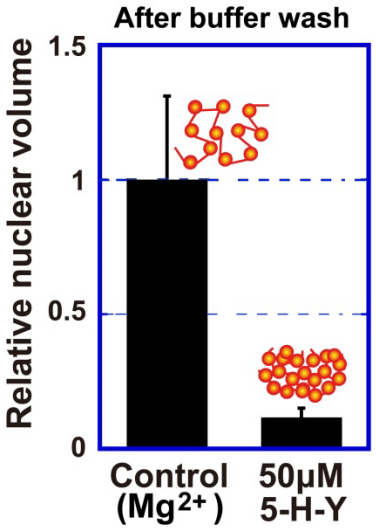

Figure 24. Volumes of Mg^{2+}-pretreated and 5-H-Y-pretreated nuclei after buffer washing. When the volume was normalized by Mg^{2+}-pretreated nuclei, although Mg^{2+}-pretreated nuclei became large after the washing (relative nuclear volume = 1), 5-H-Y-pretreated nuclei did not change (~0.1). 5-H-Y seems to bind tightly to chromatin DNA, in contrast to Mg^{2+}. The error bars represent the standard deviation.

Next, I tested whether 5-H-Y could condense chromatin *in vivo* (Figure 25). To clearly visualize the chromatin condensation *in vivo*, chromatin in HeLa cells was decondensed by treatment with the HDAC inhibitor trichostatin A (TSA) (Toth et al, 2004). When treated with 5-H-Y, the HeLa cells showed prominent chromatin condensation, especially around the nuclear periphery and nucleoli in the cells (Figure 25). However, control and cisplatin-treated cells showed less or no condensation. Taken together, these *in vitro* and *in vivo* tests demonstrate that tight DNA binding by 5-H-Y induces chromatin condensation whereas cisplatin does not.

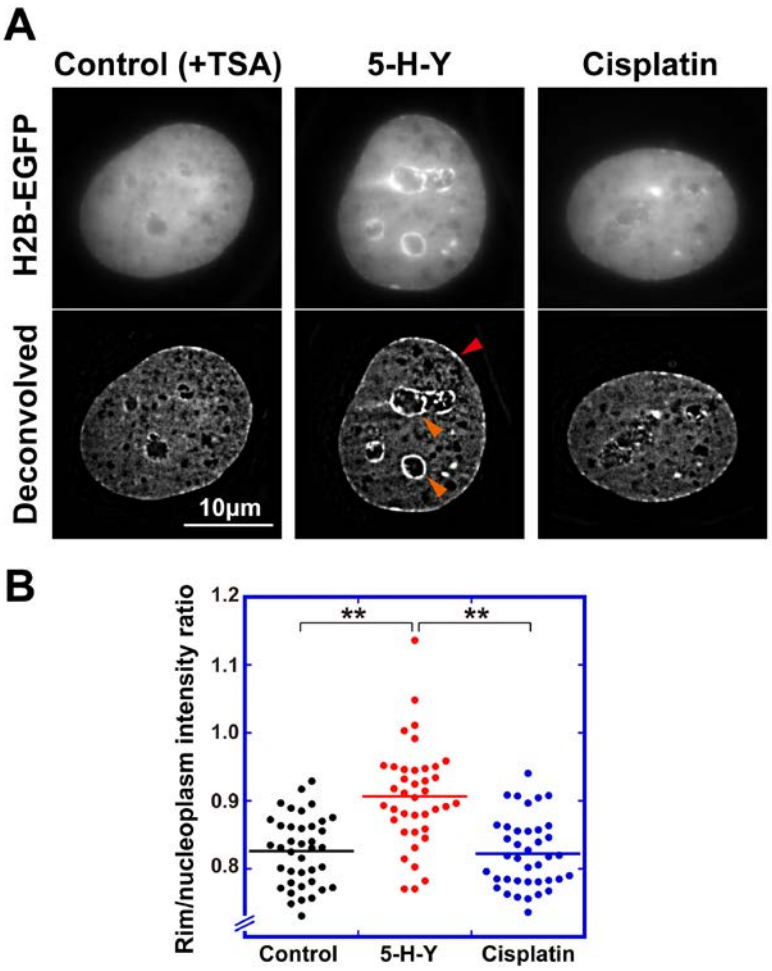

Figure 25. 5-H-Y induces chromatin condensation *in vivo*.
(A) HeLa cells were treated with TSA to decondense chromatin and then with 5-H-Y. 5-H-Y induced enrichment of chromatin at nuclear periphery (red arrowhead) and nucleoli (orange arrowheads) although I cannot exclude the possibility that condensation by 5-H-Y only occur around nucleoli and nuclear periphery. (B) The plot shows the intensity quantification of nuclear periphery chromatin. **$p < 0.01$, Chi-square test.

DNA damage by 5-H-Y is repaired primarily by different pathways than ICL repair

The results above suggest that 5-H-Y acts on DNA differently from cisplatin. Cisplatin shows hypersensitivity in cells that are deficient in the FANC genes, the products of which are involved in ICL repair. Thus, I examined whether 5-H-Y had a different reaction in such cells. For this purpose, as collaboration with Prof. Masato Kanemaki at

NIG, chicken DT40 cells were used, the genes of which can be modified efficiently using homologous recombination-mediated targeting (Buerstedde & Takeda, 1991).

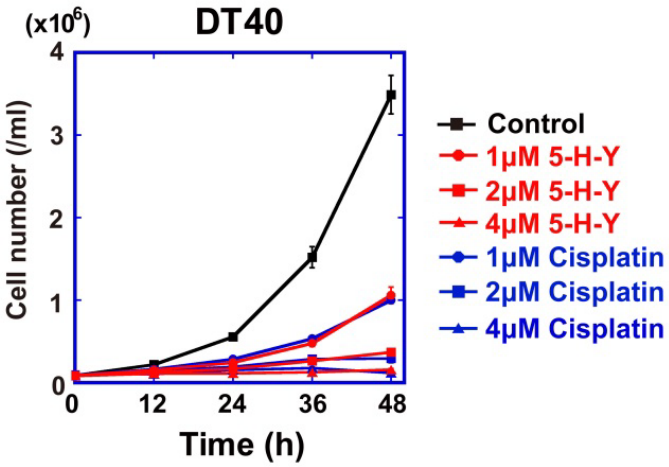

Figure 26. Cell proliferation of chicken DT40 cells upon 5-H-Y or cisplatin treatment.
The cell numbers were monitored from 0 to 48 h for DT40 cells.

5-H-Y and cisplatin inhibited wild-type DT40 cell growth in a similar manner (Figure 26). Then I examined the cell viability of DT40 cells lacking one of the FANC genes, FANCD2, by colony formation assays in the presence of 5-H-Y or cisplatin (Yamamoto et al, 2005). FANCD2-KO cells showed no hypersensitivity to 5-H-Y while just 2 μM cisplatin was enough to completely inhibit colony formation (Figure 27). A similar tendency was also observed using the FANCC- and FANCJ-KO DT40 cells although they seem to be more sick and more sensitive to any perturbations than FANCD2-KO cells (Hirano et al, 2005; Kitao et al, 2011) (Figures 28 and 29). Taken together with the *in vitro* data, these results demonstrated that 5-H-Y has a different cytotoxic mechanism than cisplatin: DNA damage by 5-H-Y is repaired by different pathways from ICL repair.

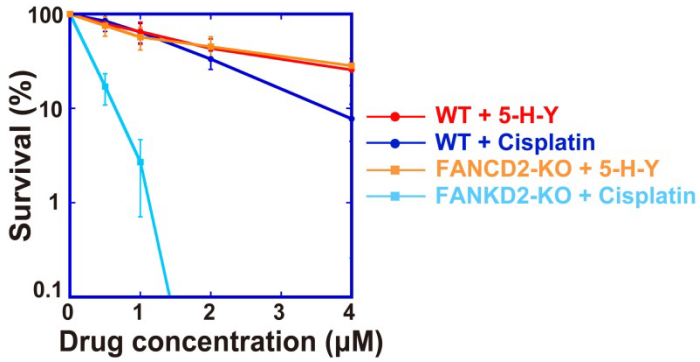

Figure 27. Sensitivity assay to the drugs in FUNCD2-KO cells using a colony formation assay. Mean ± SD of three independent experiments is shown.

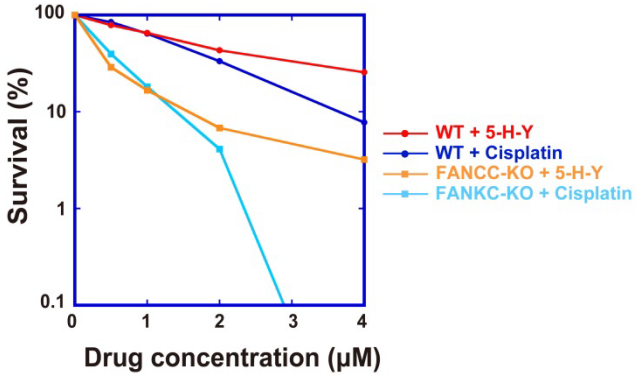

Figure 28. Sensitivity assay to the drugs in FUNCC-KO cells using a colony formation assay. Mean ± SD of three independent experiments is shown.

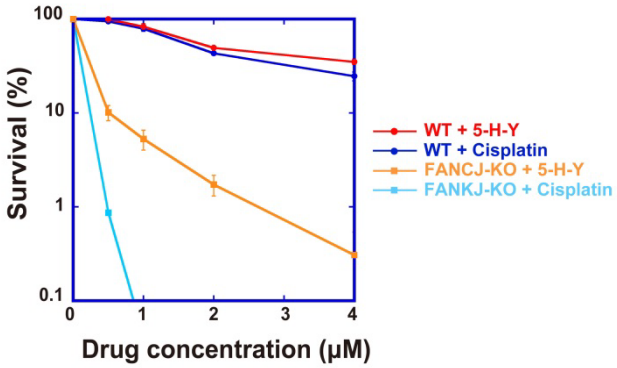

Figure 29. Sensitivity assay to the drugs in FUNCJ-KO cells using a colony formation assay. Mean ± SD of three independent experiments is shown.

Furthermore, 5-H-Y can be effective in cells with acquired resistance to cisplatin (Figure 30). Generally, tumor cells with the BRCA2 mutation show hypersensitivity to ICL-inducing agents, such as cisplatin (Yuan et al, 1999). However, such tumor cells ultimately develop cisplatin resistance (Sakai et al, 2008). For example, a BRCA2-mutated breast cancer cell line, HCC1428, partially acquired resistance to cisplatin by a secondary genetic change in BRCA2 that rescued BRCA2 function (Sakai et al, 2008). I found that HCC1428 cells still had higher sensitivity to 5-H-Y than cisplatin (Figure 30). Consistently, a previous report showed that 5-H-Y killed cisplatin−resistant types of PC-9 and PC-14 cells more efficiently than cisplatin(Uemura et al, 2012). These findings suggest that 5-H-Y can effectively suppress proliferation of cisplatin-resistant cancer cells.

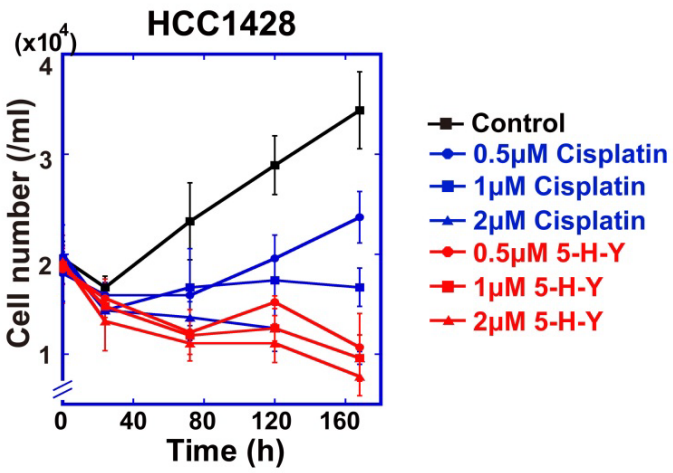

Figure 30. Cell proliferation of cisplatin-resistant HCC1428 cells upon 5-H-Y or cisplatin treatment. HCC1428 cells were treated with the indicated concentrations of 5-H-Y or cisplatin, and cell numbers were monitored. 5-H-Y was effective even in this cisplatin-resistant cell line.

1.3. Discussion

Using various techniques, it was demonstrated that the azolato-bridged complex 5-H-Y is incorporated into nuclei (Figure 1) and inhibits DNA replication and RNA transcription, arresting the treated cells in the S/G2 phase (Figures 6-8, 31). 5-H-Y binds tightly to chromatin DNA and clearly induces chromatin condensation *in vitro* and *in vivo* (Figures 20-25, 31). In addition, 5-H-Y has much less intra- and inter-strand crosslinking ability than the commonly used anti-cancer drug cisplatin (Figures 15-18). These results are consistent with genetic data that have shown that DNA damage induced by 5-H-Y is not processed by the FA/BRCA pathway, which plays an important role in the repair of cisplatin-induced ICL (Figures 27-29). Moreover, 5-H-Y can suppress proliferation of cisplatin-resistant cancer cells (Figure 30) (Uemura et al, 2012). This study provides a mechanistic insight into the differences between 5-H-Y and cisplatin. 5-H-Y may be effective against chemotherapy-insensitive cancers, especially against platinum-refractory cancers, and could be a promising alternative to platinum-based drugs.

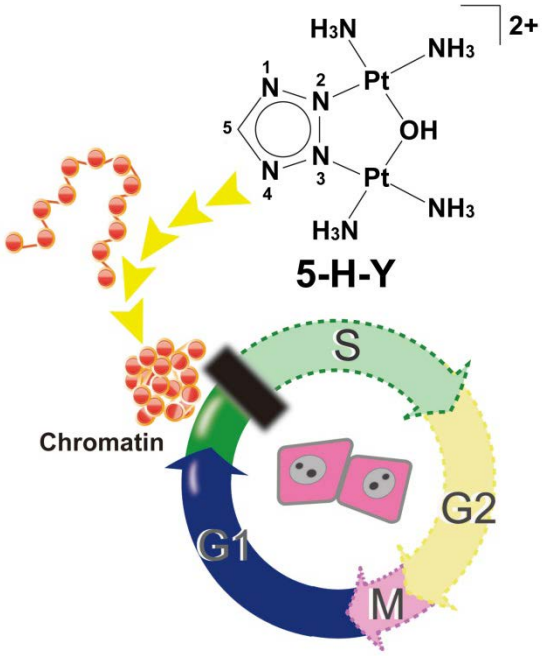

Figure 31. A model figure of this study.
This study demonstrated that 5-H-Y inhibited DNA replication, and arrests the treated cells in S/G2 phase. 5-H-Y binds tightly to chromatin DNA and induces chromatin folding in vitro and in vivo.

Regarding the inhibition mechanisms of DNA replication and RNA transcription, chromatin condensation by 5-H-Y could contribute to the processes. Although the higher-order chromatin structure is not fully understood, recent evidence suggests that interphase chromatin forms numerous condensed chromatin domains (Albiez et al, 2006; Dekker & Heard, 2015), consisting of irregularly folded nucleosome fibers (Fussner et al, 2011; Joti et al, 2012; Maeshima et al, 2010a; Maeshima et al, 2014). Because DNA replication and RNA transcription might occur at opened chromatin at the surface or outside of such compact domains (Maeshima et al, 2015; Markaki et al, 2010; Niedojadlo et al, 2011), I propose that 5-H-Y can inhibit the opening of chromatin and subsequent initiation processes in treated cells.

Another possibility is that the tight binding of 5-H-Y to chromatin DNA and

stabilization of the DNA duplex inhibit the DNA replication and RNA transcription processes directly. Recently, one azolato-bridged complex, $[\{cis\text{-}Pt(NH_3)_2\}_2(\mu\text{-}OH)(\mu\text{-pyrazolato})]^{2+}$, was shown to stay in the AT-tract minor groove of DNA by non-covalent interactions (unpublished result, Komeda et al.). 5-H-Y may also be a minor-groove binding agent and may act in a similar way to minor-groove binders such as netropsin and distamycin A (Zimmer & Wähnert, 1986), which can stabilize the DNA duplex to suppress the unwinding of DNA, a critical first step in the DNA replication and RNA transcription.

Inhibition of DNA replication by non-covalent DNA binding could be advantageous over other cancer chemotherapy agents, because covalent modification of DNA may alter genomic information (the DNA sequence) during the DNA repair process in an irreversible way, leading to the production of abnormal proteins and also drug-induced tumorigenesis. Given that cytotoxicity by 5-H-Y is assumed to change less genome DNA sequences in non-cancer cells, genome integrity could be maintained better in such cells. Efficient PCR amplification using 5-H-Y-treated template DNA (Figures 18 and 19) supports this notion.

This study has provided a mechanistic insight into the actions of 5-H-Y, which are directly related to its effects on cisplatin-resistant cancer cells and in vivo antitumor efficacy against chemotherapy resistant cancers, such as pancreatic cancer. Azolato-bridged complexes are among the most promising anticancer drug candidates.

1.4. Materials and Methods

Chemicals

5-H-Y was prepared as reported previously (Komeda et al, 2011). Cisplatin was purchased from Bristol-Myers Squibb.

Cell lines

Human cell lines PC9, HeLa, U2OS, and TIG-1, except HCC1428 were maintained in Dulbecco's modified Eagle's medium (GIBCO) supplemented with 10% (v/v) fetal bovine serum (Thermo Scientific) at 37°C under 5% CO_2 in air in a humidified incubator. HCC1428 cells were maintained in RPMI1640 medium supplemented with 10% FBS. Chicken DT40 cells were cultured in DMEM/high glucose medium (Sigma) supplemented with 10^{-5} M β-mercaptoethanol (Sigma), 100 U/mL penicillin, 100 mg/mL streptomycin (GIBCO), 10% fetal calf serum (Hana-Nesco Bio), and 1% chicken serum (GIBCO) at 38.5°C.

Cell proliferation assay

Cells were seeded in 6-well plates (1×10^5 or 2×10^4 cells/mL) with various concentrations (0–4 μM) of 5-H-Y or cisplatin. The numbers of proliferated viable cells were examined microscopically at several time points, as indicated in each figure.

Measurement of cellular platinum by ICP-MS

PC9 cells were harvested 24 h after the addition of cisplatin or 5-H-Y. I washed out dead cells and harvested only living cells. To purify whole cells, I centrifuged the cell suspension and collected the cells. To obtain the nuclear fraction, cells were suspended

in HBSS buffer containing 0.2 mM phenylmethylsulphonyl fluoride (PMSF) and 0.1% Triton X-100. Then the nuclei were collected by centrifugation. To isolate the DNA fraction, I performed the following procedure. I treated whole cells with SDS to lyse the cells, and then the lysate was treated with proteinase K (WAKO). DNA was isolated from the lysate by phenol-chloroform extraction and ethanol precipitation, then redissolved in MilliQ water. Then the solution was treated with 0.04 mg/mL RNaseA. The DNA was purified by phenol-chloroform precipitation and ethanol precipitation again and finally redissolved in TE buffer (pH 8.0). Each fraction was snap-frozen in liquid nitrogen. As blanks, I performed all of the fractionation steps in the absence of any cells. To measure Pt, the fractions were subjected to inductively coupled plasma mass spectroscopy (ICP-MS; Toray Research Center, Shiga, Japan).

Cell viability assay

Serially diluted cells were plated in medium containing 1.5% methylcellulose. To measure sensitivity to 5-H-Y or cisplatin, exponentially growing cells were incubated in methylcellulose medium with the drugs. Colonies were counted after incubation for 1–2 weeks.

Flow Cytometry

For flow cytometry (FCM), cells treated with 5-H-Y or cisplatin for 24 h were pulse-labeled for 60 min with 10 μM 5-ethynyl-2’-deoxyuridine (EdU). The dead cells were washed away prior to the cell harvest. After harvesting, to fluorescently label the incorporated EdU in newly synthesized DNA, I used Click-iT EdU Flow Cytometry Assay kits (Invitrogen). The cells were also stained with FxCycle Far Red Stain

(Invitrogen) to stain DNA. FCM analysis was performed with a JSAN cell sorter (Bay Bioscience) using a logarithmic FL1-A channel for EdU detection and a linear FL5-A setting for FxCycle Far Red Stain. The cells with abnormal shapes or multiple nuclei were eliminated by forward/sideward scatter (FSC/SSC) gating. Analysis was performed using the Flowlogic software. For each analysis, I started with ~10^6 cells and ~10^4 cells of the flow cytometer result were plotted.

In vivo measurement of RNA transcription

HeLa cells on coverslips were cultured with 2 μM of 5-H-Y or cisplatin for 24 h and in the last 1 h with 50 μM of EU. The cells were then treated with 3.7% formaldehyde and then with 0.5% triton X-100 for permeabilization. Incorporated EU was fluorescently labeled by Click-iT reaction (Invitrogen) using Click-iT Alexa Fluor 594 dye. DNA was then stained with 0.5 μg/ml DAPI. The mounted cells were observed under a DeltaVision microscope (Applied Precision) and analyzed using the ImageJ software (NIH, Bethesda, MD, USA) (Schneider et al, 2012).

Immunofluorescence staining and immunoblotting

Immunofluorescence staining was performed as described previously. The primary antibody, anti-phospho H2AX (Ser139) mouse monoclonal (Upstate), and the secondary antibody, Alexa-Fluor-594-conjugated goat anti-mouse IgG (Invitrogen), were used at dilutions of 1:3000 and 1:1000, respectively. The samples were analyzed under a DeltaVision microscope (Applied Precision). Images were analyzed using the ImageJ software(Schneider et al, 2012).

For immunoblotting, the following antibodies were used at the indicated dilutions: anti-phospho Chk1 (Ser345) rabbit polyclonal (Cell Signaling Technology, Inc.) at 1:500, anti-Chk1 mouse monoclonal (MBL) at 1:1000, anti-histone H2B rabbit polyclonal (upstate) at 1:10000, horseradish peroxidase-linked anti-rabbit IgG whole antibody (Bio-Rad) at 1:5000 for anti-phospho Chk1 and at 1:30000 for anti-histone H2B, and horseradish peroxidase-linked anti-mouse IgG whole antibody (Bio-Rad) at 1:5000. Cells were lysed in FSB buffer. After denaturation at 95°C for 5 min, proteins in lysates were separated using SDS-PAGE. Proteins were transferred to an Immobilon-P membrane (Millipore) and blotted with antibodies after blocking in PBS-T containing 5% BSA for staining phospho-Chk1 and 3% skim milk for staining Chk1and H2B for 30 min at RT. Detection was performed using the Immobilon Western Chemiluminescent HRP substrates (Millipore) with EZ-Capture MG (ATTO).

Scanning X-ray fluorescence microscopy (SXFM)

SXFM was set up at an undulator beamline, BL29XU, of the SPring-8 synchrotron radiation facility in Japan by combining a Kirkpatrick-Baez type X-ray focusing system (Kirkpatrick & Baez, 1948; Yamauchi et al, 2003), an *xy*-scanning stage for sample mounting, and an energy-dispersive X-ray detector (Vortex-90EX, Hitachi High-Technologies Science America, Inc.). For element array analysis, monochromatic X-rays at 15 keV for Pt *L*-line excitation were focused into a 1000 nm (H) × 1000 nm (W) spot with a measured flux of ~3×10^{11} photons/s. The focused X-rays simultaneously yielded the fluorescence of various chemical species in a small volume of sample cells. The X-ray fluorescence spectrum was recorded with an exposure of 4–10 s at each pixel of scanning. The fluorescence signals of each element of interest were

extracted and normalized by incident beam intensity. After scanning the whole area, elemental distributions were visualized digitally. In addition to the mapping images, an elemental concentration was analyzed quantitatively using thin platinum films, of which the thickness and the density were determined in advance. PC9 cells were plated on acrylic-based prolene film with carbon deposition (Jeol, Tokyo, Japan), which were washed three times with 70% EtOH (Wako Pure Chemical, Osaka Japan). After cells had adhered well, platinum compounds were treated for 24 h. After fixation with 2% paraformaldehyde in phosphate-buffered saline (PBS) for 10 min, cells were washed once in PBS prior to washing with 70% EtOH and dried. Note that dead cells were washed out and only living cells were fixed.

Measurement of cellular elements by ICP-MS or HPLC-ICP-MS

To determine the metal concentration of platinum in whole cells or cellular fractions, about ~5×10^6 cells were wet-digested with 1.0 mL HNO_3 at 160°C for 12 h. Concentrations of ^{194}Pt and ^{195}Pt were determined by the ICP-MS (ELAN DRC II, Perkin Elmer, MA, USA).

Sedimentation Velocity of Nucleosomal Arrays and 5-H-Y

Nucleosomal arrays were assembled as described (Hansen & Lohr, 1993), using a 12-mer 601 (Lowary & Widom, 1998) DNA template and native chicken core histone octamers (Hansen et al, 1989). Samples were prepared for the analytical ultracentrifuge by diluting to an absorbance of approximately 0.6 at 260 nm, and the 5-H-Y or Cisplatin added to the appropriate concentration.

Sedimentation velocity experiments were conducted in a Beckman XL-A/I analytical ultracentrifuge at 17,000 RPM using absorbance optics as described (Schwarz & Hansen, 1994). The scans were analyzed using the enhanced van Holde-Weischet method(Van Holde & Weischet, 1978) implemented in the Ultrascan II data analysis software (Demeler, 2005) to yield an integral distribution of diffusion-corrected sedimentation coefficients.

Chromatin compaction assay by measurement of nuclear volume

For condensed chromatin, isolated nuclei (~1×10^7) were suspended in HM buffer (10 mM HEPES-KOH, pH 7.4, and 5 mM $MgCl_2$) and attached to poly L-lysine-coated coverslips by centrifugation (400×*g*, 5 min) (Takata et al, 2013). For decondensed chromatin, the nuclei on the coverslips were gently transferred to HM buffer or 1 mM EDTA buffer (pH 8.0). The nuclei were treated with 5-H-Y overnight at room temperature in the dark. Hereinafter, all solutions included 5-H-Y. After fixation with 1% formaldehyde, the nuclei were washed with 50 mM glycine and stained with 2 μM TO-PRO-3 solution (Invitrogen) at 37°C for 30 min. After washing, *z*-stack images were acquired using an LSM510 META laser scanning confocal microscope (Carl Zeiss, Wetzlar, Germany) with a 100× objective at 0.48 μm intervals. The images were processed using the LSM Image Browser (Carl Zeiss) and ImageJ software(Schneider et al, 2012).

To examine whether buffer washing removed 5-H-Y from chromatin, 5-H-Y-pretreated chromatin or 5 mM Mg^{2+}-pretreated chromatin were further washed with 1 mM EDTA without 5-H-Y three times. Then, nuclear volumes were measured as described above

and normalized by the average volume of 5 mM Mg^{2+}-pretreated nuclei.

Observation of chromatin compaction in vivo

At first, notable effect on chromatin in the 5-H-Y-treated cells were not seen, presumably because of the resolution limitation by a conventional light microscopy. To enhance a possible effect, the cells were first treated with 500 nM trichostatin A (TSA) for 4 h to decondense chromatin in the cells (e.g. (Toth et al, 2004)). Then 10 μM 5-H-Y or cisplatin was added to the TSA-treated cells and further incubated for 1 h. The cells were observed by live cell imaging with a fluorescent microscope (Nikon Eclipse Ti2000-E). I used oblique illumination microscopy (Hihara et al, 2012; Tokunaga et al, 2008). For the quantification of condensation, fluorescent intensity of the nuclear rim (average width of 5 pixels, 320 nm) and the nucleoplasm (average width of 10 pixels, 640 nm) were measured by line scan method. The induced condensation was evaluated by the ratio of nuclear rim intensity to nucleoplasm intensity. These analyses were performed with the ImageJ software (Schneider et al, 2012). The statistical significance was evaluated by Chi-square test.

Quantitation of covalent Pt-DNA adducts

Double-helical calf-thymus (CT) DNA solutions (100 μM, relative to the monomeric nucleotide content) were incubated with 8 μM cisplatin or 5-H-Y in a buffer solution composed of 10 mM HEPES (pH 7.5), 100 mM $KClO_4$, and 2 mM $MgCl_2$ at 37°C. At various time intervals, an aliquot (500 μL) of the reaction mixture was withdrawn, and 100 μL 4 M NH_4Cl was added to each reaction mixture immediately after sample collection to prevent further platination. Then each sample solution was poured into a

cation exchange SPE tube (Discovery DSC-WCX SPE Tube, SUPELCO), which was washed with 250 μL MilliQ water twice and then multiple steps of ultrafiltration (1,000 *g*, 4°C, 6–7 min) were performed to remove non-covalently bound platinum complexes from the eluate, using a centrifugal ultrafiltration device (Nanosep and Nanosep MF Centrifugal Devices, Pall) after adding the following solutions: 250 μL 4 M NH_4Cl (three times), 25 μL 4 mM EDTA, 25 μL 4 M NaOH and MilliQ water to a final volume of 500 μL including DNA solution (once), 250 μL 4 M NH_4Cl (three times), and 250 μL MilliQ water (three times). After ultrafiltration, the total monomeric nucleotide content of covalently platinated CT DNA in each sample solution was determined by measuring UV absorbance at 260 nm using a spectrophotometer (GeneQuant, GE Healthcare). Then each DNA solution was sonicated, washed in concentrated HNO_3, and redissolved in 2% HNO_3 for ICP-MS measurements (Agilent 7500cs, Agilent Technology) to determine the platinum content in the DNA. The R_b value, defined as the molar ratio of platinum complex bound per nucleotide, was calculated from the DNA and platinum content in each sample.

PCR using drug-treated plasmid DNA

pUC19 and pBluescript II were linearized by *Eco*RI digestion, recovered by ethanol precipitation, and treated with 2.5 μM cisplatin or 5-H-Y (DNA base:drug = 30:1) for 24 h or 48 h at 37°C. After purification using Wizard SV Gel and the PCR Clean-Up System (Promega), 50 ng purified plasmid was used as templates for PCR with the following set of primers: primer F, AGCAAAAACAGGAAGGCAAA and primer R, ACTGGCCGTCGTTTTAC. PCR was performed with the KOD-Plus kit (Toyobo) according to the manufacturer’s protocol. The cycle numbers used were 4, 7, and 10

cycles. The PCR products were electrophoresed on 0.8% agarose gels and stained with EtBr to visualize DNA.

Alkaline agarose electrophoresis

To detect inter-strand crosslinks in drug-treated DNAs, alkaline agarose gel electrophoresis was carried out. pUC19 and pBluescript II were linearized by *Eco*RI digestion, recovered by ethanol precipitation, and treated with 2.5 μM cisplatin or 5-H-Y (DNA base:drug = 30:1) for 24 h or 48 h at 37°C. After purification using Wizard SV Gel and the PCR Clean-Up System (Promega), 1 μg of each purified plasmid was mixed in a buffer containing 50 mM NaOH, 1 mM EDTA (pH 8.0), 3% (w/v) Ficoll, and 0.0425% (w/v) xylene cyanol. The plasmid samples were electrophoresed on 0.8% alkaline agarose gel in 50 mM NaOH and 1 mM EDTA (pH 8.0). After electrophoresis, the gel was neutralized in a buffer containing 1 M Tris-HCl (pH 7.6) and 1.5 M NaCl for 45 min and stained with 0.3 μg/mL EtBr in 1× TAE buffer (40 mM Tris, 20 mM sodium acetate, and 1 mM EDTA, pH 8.0).

Nocodazole-thymidine block for synchronization of the cells at G1/S phase

Unsynchronized HeLa cells were treated with 80 ng/mL nocodazole for 4 h. After synchronization at the mitotic phase, mitotic cells were isolated by shaking off and were incubated in medium containing 2.5 mM thymidine to block the cells in the G1/S phase. Then, 4 h later, 2 μM 5-H-Y or cisplatin was added to thymidine-containing medium and the cells were incubated for a further 15 h. Then the synchronized cells were released from the thymidine block and labeled with 10 μM EdU for 1or 3 h (see also Figure 9). Harvesting and staining for FCM were the same as for unsynchronized cells.

In vivo EdU labeling

Cells were seeded on poly-L-lysine-coated coverslips. The cells were treated with 10 μM of 5-H-Y or cisplatin for 1 h. 5 μM EdU was added to the drug-treated cells and further incubated for 1 h. The cells were then fixed with 1.85% formaldehyde and permeabilized with 0.5% triton X-100. Incorporated EdU was labeled by Click-iT reaction (Invitrogen) using EdU Alexa Fluor 594 dye. DNA was stained with 0.5 μg/ml DAPI. The mounted cells were observed under a DeltaVision microscope (Applied Precision) and analyzed using the ImageJ software.

Chapter 2

Density imaging of heterochromatin in live cells using orientation-independent-DIC microscopy

2.1. Introduction

As discussed in the previous chapter, growing evidence has suggested that the nucleosomes, consisting of DNA wrapped around core histones (Luger et al, 1997), are rather irregularly folded without the regular chromatin fibers in eukaryotic cells(Chen et al, 2016; Fussner et al, 2012; Hsieh et al, 2015; Joti et al, 2012; Maeshima et al, 2014; Ou et al, 2017; Ricci et al, 2015; Sanborn et al, 2015). Super-resolution fluorescence microscopy and chromosome conformation capture (3C) derivatives such as Hi-C have revealed the existence of various chromatin domains, such as topologically associating domain (TAD), in the cell (Boettiger et al, 2016; Cremer et al, 2017; Dixon et al, 2012; Eagen et al, 2015; Markaki et al, 2010; Nora et al, 2012; Nozaki et al, 2017; Rao et al, 2014; Sexton et al, 2012).

According to typical textbook models, chromatin can be categorized into two types ("euchromatin" and "heterochromatin") based on its degree of compaction (Alberts et al, 2007; Pollard et al, 2016). These two types of chromatin were originally observed in 1928 by Heitz (Heitz, 1928), and were described as sparse and dense chromatic regions. Heterochromatin has been further grouped into constitutive and facultative types, each

of which plays a distinct role in the regulation of genomic functions (Brown, 1966; Trojer & Reinberg, 2007).

Constitutive heterochromatin is typically gene-poor, usually possesses AT-rich repetitive DNA sequences, and has a highly condensed structure (Maison et al, 2010; Saksouk et al, 2015). It provides structural functions in areas such as chromosome centromeres or telomeres and replicates in the mid-to-late S phase. Masses of pericentric heterochromatin in mouse interphase cells, often called “chromocenters” (Guenatri et al, 2004), have been extensively studied as a constitutive heterochromatin model. Pericentric heterochromatin is composed of highly clustered major satellite repeat sequences (several Mb of 234 base pair [bp] units) associated with centromeres, and is highly condensed and easily detectable by DNA staining as large 4',6-diamidino-2-phenylindole (DAPI)-dense foci (Maison et al, 2010; Saksouk et al, 2015). The signal intensity of foci by DAPI staining is 6-fold higher than that in surrounding regions (Bancaud et al, 2009), and is marked with heterochromatin protein 1 (HP1) (Grewal & Jia, 2007; Maison et al, 2010), MeCP2 (Brero et al, 2005; Nan et al, 1996), and tail methylation of histone H3 (H3K9me3) (Allis & Jenuwein, 2016).

Facultative heterochromatin corresponds to genetic regions that are silenced through a mechanism involving histone modification or RNA binding (Trojer & Reinberg, 2007; Wutz, 2011). It is not repetitive, and shares some features of constitutive heterochromatin. Importantly, under specific developmental or environmental conditions, facultative heterochromatin can lose its condensed structure and become transcriptionally active. A famous process involving facultative heterochromatin is

X-inactivation, through which one of the copies of the X chromosome present in female mammals is transcriptionally silenced, creating a Barr body (da Rocha & Heard, 2017; Jegu et al, 2017; Nakajima & Sado, 2014; Smeets et al, 2014; Wutz, 2011).

Although the heterochromatin is generally well condensed, it does not completely prevent protein diffusion (Cremer et al, 2015). For example, fluorescence correlation spectroscopy (FCS) imaging detected diffusion of protein molecules into heterochromatin regions (Bancaud et al, 2009; Baum et al, 2014), as reported in condensed mitotic chromosomes (Chen et al, 2005; Hihara et al, 2012). In light of other factors, including their low levels of transcription (Saksouk et al, 2015; Trojer & Reinberg, 2007) and DNA replication in mid-to-late S phase (Guenatri et al, 2004; Wu et al, 2006), heterochromatin regions seem to pose only a moderate barrier to protein access. To determine what is responsible for such a barrier, it is critical to not only characterize the molecular components of heterochromatin including histone modifications, specific proteins, and RNAs (Allis & Jenuwein, 2016; Grewal & Jia, 2007; Maison & Almouzni, 2004; Saksouk et al, 2015), but also to investigate the physical properties of heterochromatin, such as its density in live cells. We could relatively easily obtain DNA density information in the heterochromatin as described above (Bancaud et al, 2009), and also from the recent volume analyses on specific regions in heterochromatin using a combination of super-resolution imaging, chromatin immunoprecipitation sequencing (ChIP-seq), and DNA-fluorescence in situ hybridization (FISH) techniques (see Results) (Boettiger et al, 2016; Wang et al, 2016). However, to understand the moderate access barrier mechanism we also need to know the total density, including non-nucleosomal material (proteins, RNAs) in the

heterochromatin of live cells.

While elucidating such physical properties in live cells is technically challenging, it can be achieved through differential interference contrast (DIC) microscopy (Inoué & Spring, 1997; Oldenbourg, 2010), a common tool in cell biology research. DIC images are produced by the interference of two laterally displaced light beams passing through a sample (e.g., live cells), capturing information about the optical path length in the sample to reveal otherwise invisible features (Allen et al, 1969). The difference in optical path length between the two beams provides contrast to the image, which reflects local differences in the refractive index within the sample. However, contrast in DIC images depends on the direction of displacement between the two light beams and the sample, also called the "shear direction," precluding quantitative measurement of the optical path length.

To overcome the limitations of DIC systems, an orientation-independent differential interference contrast (OI-DIC) microscopy method was developed (Shribak, 2013). OI-DIC microscopy allows the directions of displacement for the two light beams to be switched rapidly without mechanically rotating the sample or the prisms, generating a quantitative optical path difference (OPD) map. Based on the OPD value, it is possible to estimate the density of intracellular components in live cells.

Using OI-DIC microscopy, I focused on the pericentric heterochromatin foci (chromocenters) in live mouse NIH3T3 cells. I quantified the absolute density of the materials in the pericentric foci and surrounding regions, which are putatively

euchromatic and free from MeCP2 and H3K9me3 heterochromatic marks. The quantification showed that the density of the heterochromatin was 208 mg/mL, only 1.53-fold higher than that of the surrounding euchromatic regions (136 mg/mL). Surprisingly, this difference was much smaller than that obtained from fluorescence staining of genomic DNA (5.5–7.5-fold). These results, as well as further analysis, suggested that non-nucleosomal materials (proteins, RNAs), which can contribute to chromatin compaction through the macromolecular crowding effect (Asakura & Oosawa, 1954; Hancock, 2007; Marenduzzo et al, 2006), were dominant in both heterochromatin and euchromatin (~ 120 mg/mL). Further computational simulation suggested that the non-nucleosomal materials help create a moderate barrier to the diffusion of proteins to heterochromatin, where they dynamically regulate heterochromatin functions. The results of this study reveal a novel aspect of heterochromatin in live cells related to its density.

2.2. Results

Density of heterochromatin in live mouse cells was only 1.53-fold higher than that of the surrounding euchromatic regions

To estimate the density of total materials in the heterochromatin and euchromatin regions, as collaboration with Dr. Michael Shribak and Dr. Tomomi Tani at Marine Biological Laboratory (MBL), I used an OI-DIC microscopy system; the principal schematic of this system is shown in Figure 32. Based on the OPD map obtained from OI-DIC imaging (Figure 33), as well as the measured thickness of the sample (Figure 34) and refractive index (RI) of the surrounding medium, we were able to calculate the dry mass density of the sample (Figures 33-37; for more details, see Materials and Methods). Next, to evaluate whether OI-DIC imaging and subsequent analysis could accurately estimate RI, I observed glass rods (diameter = 4 μm) in a mineral oil with known RI (1.54 and 1.58) and calculated the theoretical OPD (Figures 38 and 39). We found that theoretical and optically measured OPD were almost identical (Figures 38 and 39), validating the accuracy of the OI-DIC imaging for estimating the RI of samples with measured OPD.

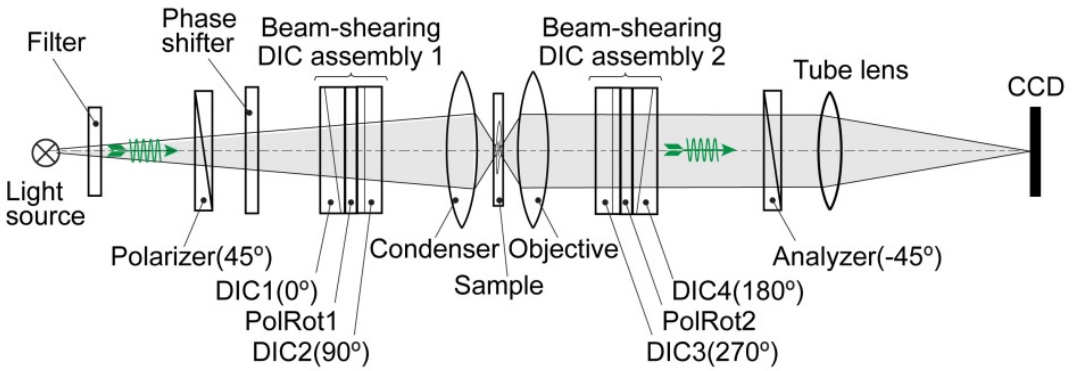

Figure 32. A schematic of the OI-DIC set-up.

Details of the microcopy system are described in the Materials and Methods section.

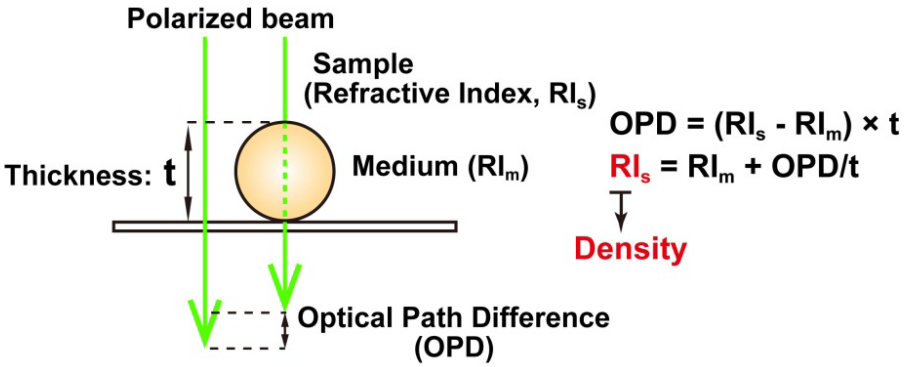

Figure 33. A procedure for estimating sample (depicted as a sphere) RI.

OI-DIC microscopy can computationally quantify OPDs at each spatial point. For details, see the Materials and Methods section.

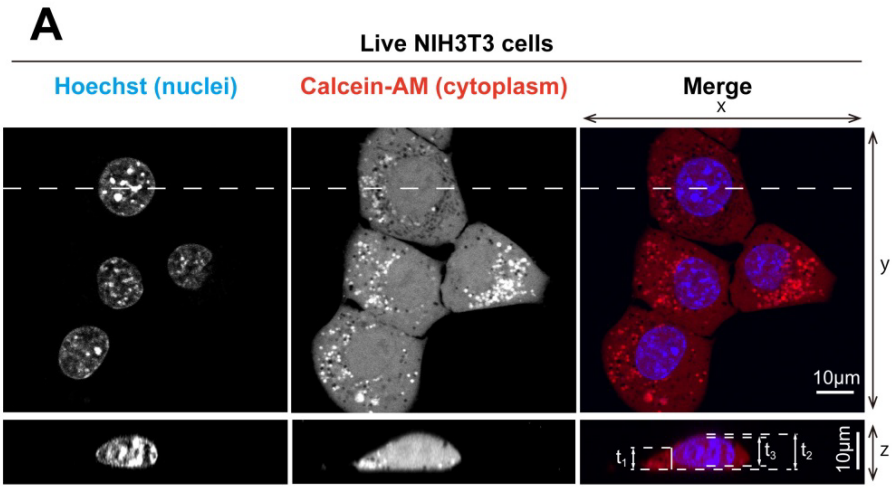

B

Thickness of each point (Median ± quartile deviation)

	t_1	t_2	t_3	
Live NIH3T3	6.35 ± 0.69	8.21 ± 0.93	6.90 ± 0.59	(n = 21)
NIH3T3 MeOH fixed	*5.65	*7.31	6.14 ± 0.87	(n = 28)
NIH3T3 FA fixed	*4.54	*5.87	4.94 ± 0.48	(n = 26)
Live RPE1	*4.54	*5.87	4.94 ± 0.62	(n = 20)

* Calculated from ratio of t_1: t_2: t_3 of NIH3T3 untreated live cells

Figure 34. The thicknesses of the cells I used in this study.
(A) Thickness measurements of nuclei and cytoplasm. DNA and cytoplasm were stained with Hoechst 33342 and Calcein-AM, respectively. x–y images (upper) and cross-sectional (x–z) images (lower) along the dashed white lines are shown. To calculate RI, three thicknesses measurements were taken: t_1, cytoplasm region adjacent to the nucleus; t_2, the thickest region of a cell, including the cytoplasm and nucleus; t_3, the thickest region of a nucleus. (B) Table of the measured thicknesses (t_1, t_2, and t_3) for each cell line and condition. The values are presented as median ± quartile deviation.

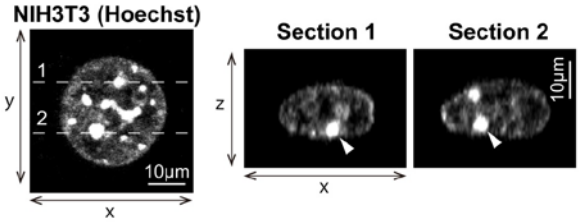

Figure 35. Cross-sectional views (center and right) of pericentric heterochromatin foci along two dashed white lines indicated in the x-y image (left).
Note that the pericentric foci (arrowheads) seem to be spherical.

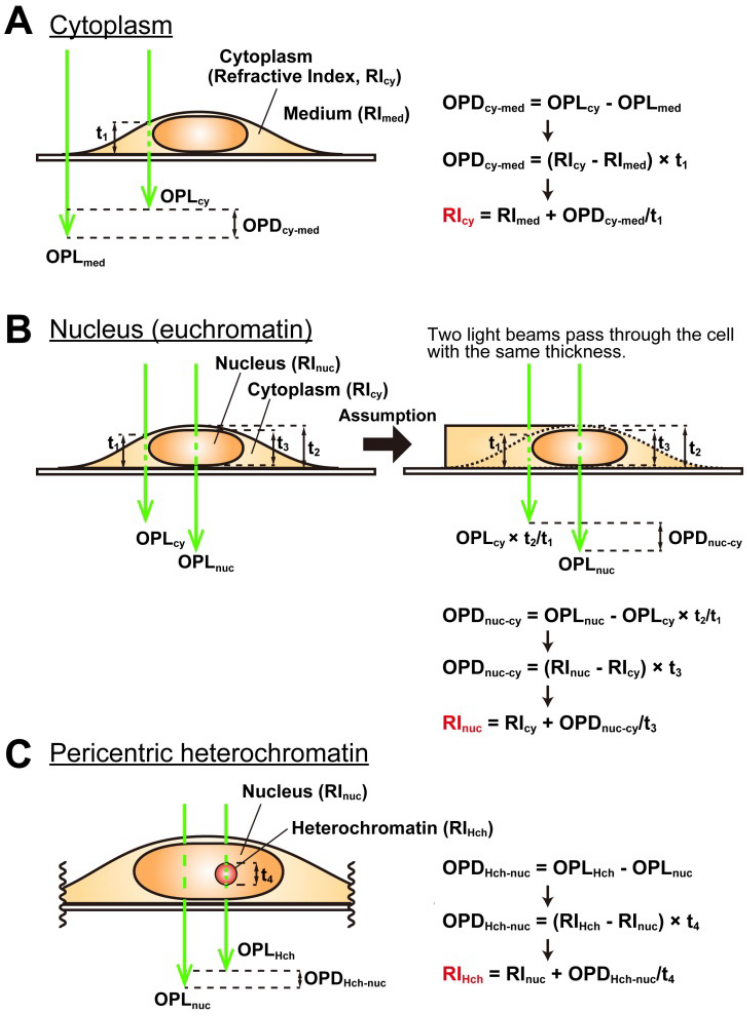

Figure 36. Schematics of how to calculate the density of each cellular compartment.
(A) A calculation scheme for the RI_{cy}. I obtained RI_{cy} based on the measured values for $OPD_{cy\text{-}med}$, thickness t_1 and RI_{med}. (B) RI_{nuc} (euchromatin). Because the thicknesses of the sample through each of the two polarized beam passed should be the same, I multiplied OPD_{cy} by t_2/t_1 to obtain $OPD_{nuc\text{-}cy}$ (t_2, thickest point of the cell including nucleus and cytoplasm; t_1, thickness of cytoplasm region beside nucleus) (see also Figure 34). RI_{nuc} was calculated based on RI_{cy} and nuclear thickness t_3. (C) Heterochromatin foci RI (RI_{Hch}). The heterochromatin focus thickness t_4 was assumed to be their width (see also Figure 35).

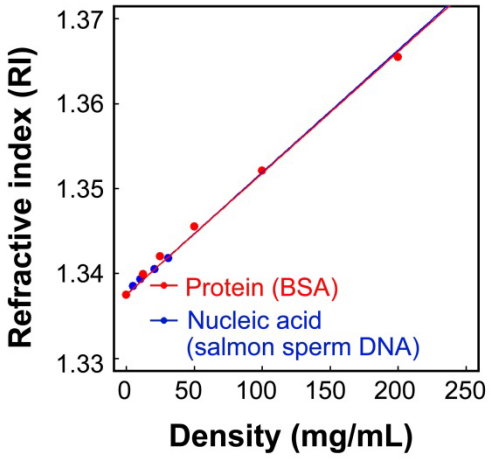

Figure 37. The calibration curve of RIs versus the density of standard solutions for protein or nucleic acid.

For details, see the Materials and Methods section. RI = 1.3375 + 1.4 × 10^{-4} (mL/mg) × C (RI, the refractive index; C, the concentration of the nucleic acids or proteins [mg/mL]).

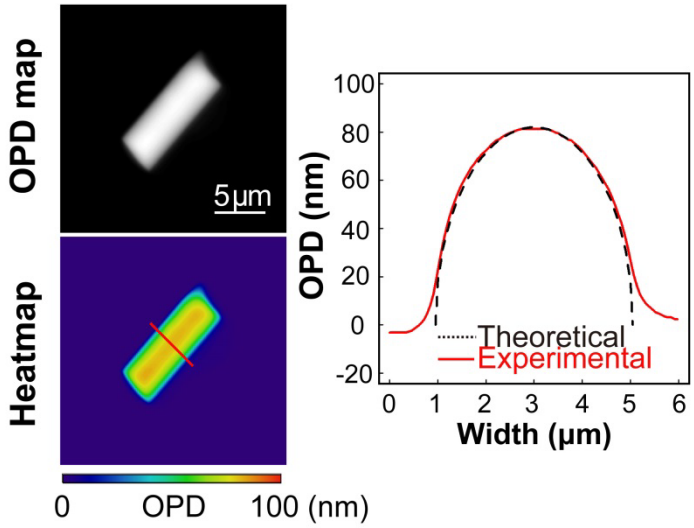

Figure 38. Validation of density imaging by OI-DIC microscopy using known glass rods and mineral oils.

The RI of the glass rods was 1.56, and that of the oil was 1.54. Note that the theoretical and experimental values were almost the same, ensuring the accuracy of RI quantification. Scale bar: 5 μm.

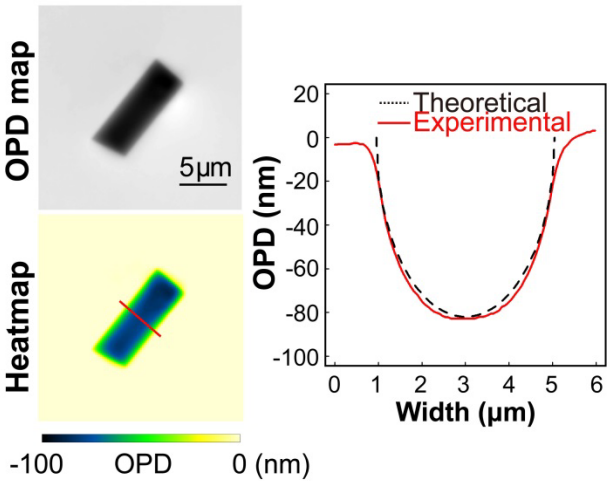

Figure 39. Validation of density imaging by OI-DIC microscopy using known glass rods and mineral oils with other RI.

The RI of the glass rods was 1.56, and that of the oil was 1.58. Similarly to the result shown in Figure 38, the theoretical and experimental values were almost the same, ensuring the accuracy of RI quantification. Scale bar: 5 μm.

Using the method described above (see also Figure 40), I performed OI-DIC imaging of live mouse fibroblast NIH3T3 cells. Cytoplasmic organelles, nuclear envelopes, and presumably nucleoli were clearly observed (Figure 41, left). Subsequent analyses mainly focused on large pericentric heterochromatin foci, which are a strong constitutive heterochromatin model. To identify the precise positions of heterochromatin foci in a nucleus, I specifically labeled the foci with enhanced green fluorescent protein (EGFP)-fused MeCP2 (Figure 41, right), which is a methylated DNA binding protein and a marker protein of constitutive heterochromatin (Brero et al, 2005; Nan et al, 1996). I confirmed that MeCP2-EGFP localized in certain regions that were strongly stained with Hoechst 33342 as foci (Figure 41, center and right).

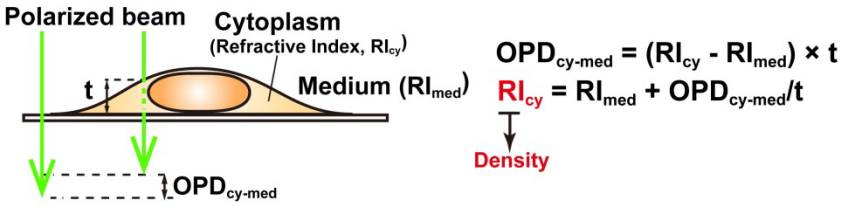

Figure 40. A simple schematic of the method to estimate the RI_{cy}.

The RI_{cy} can be calculated based on the measured RI_{med} and t values (Figures 34 and 37). For details, see Figure 36 and the Materials and Methods section.

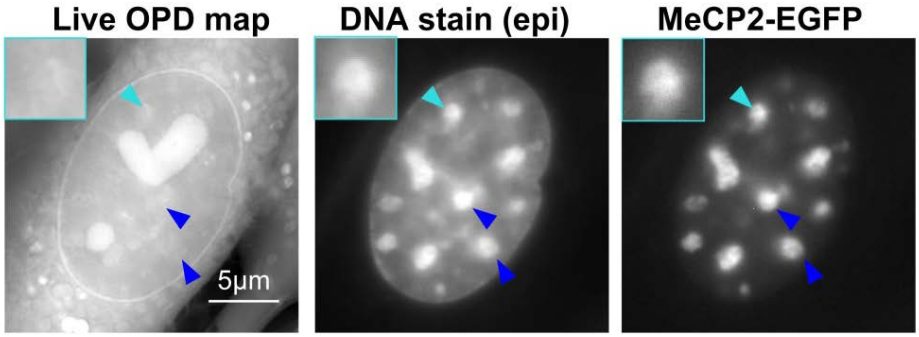

Figure 41. Typical images of the OPD map, DNA staining, and MeCP2-EGFP signals in live NIH3T3 cells.

In DNA staining and MeCP2-EGFP images, co-localized large foci (blue and cyan arrowheads) were assumed to be the pericentric heterochromatin. Note that the OPD of pericentric foci was similar to or slightly higher than that of the surrounding regions. High-intensity regions in the nuclei of OPD maps were nucleoli (Figure 48). Insets: magnified images of the foci indicated by cyan arrowheads. Scale bar: 5 μm.

After acquiring the OPD map for live NIH3T3 cells, I unexpectedly found that the OPD of the pericentric foci (arrowheads in Figure 41) was similar to or slightly higher than that of the surrounding regions. Because the surrounding regions not only exhibited much weaker Hoechst 33342 signals (Figure 41, center; Figure 42A, left) but were also nearly free of MeCP2 (Figure 42) and histone H3K9me3 marks (Figure 43) (Allis & Jenuwein, 2016), here I called them “surrounding euchromatin regions” or “euchromatin regions” (see also the Discussion). Thickness data for cytoplasm, nuclei,

and cells was obtained by confocal laser microscopy (Figure 34), which I used to estimate densities at the pericentric foci labeled with MeCP2-EGFP and the surrounding euchromatin (for details, see Figure 36; Table 1).

Table 1. Densities of cellular compartments in various cell lines/conditions (mg/mL)
(Median ± quartile deviation)

	Cytosol	Surrounding euchromatin	Heterochromatin	Nucleolus
Live NIH3T3	165 ± 18.6	136 ± 12.9	208 ± 31.3	259 ± 24.4
NIH3T3 MeOH fixed	136 ± 17.3	109 ± 15.4	289 ± 31.3	292 ± 34.1
NIH3T3 FA fixed	145 ± 8.78	144 ± 8.05	174 ± 16.5	254 ± 20.7
Live RPE-1	161 ± 6.91	137 ± 7.52	202 ± 25.2 (Inactive X)	226 ± 15.9

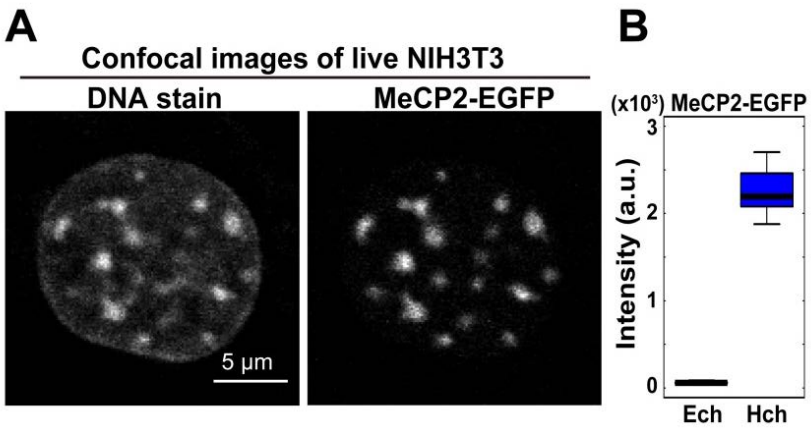

Figure 42. The enrichment of MeCP2 at pericentric foci.
(A) Confocal microscope images of DNA staining (Hoechst 33342) and MeCP2-EGFP in live NIH3T3 cells. The regions surrounding the pericentric foci seem almost free of MeCP2. Scale bar: 5 µm. (B) Difference in signal intensity between the heterochromatin (Hch) visualized by MeCP2-EGFP and the surrounding euchromatin region (Ech) in live NIH3T3 cells. The fluorescence ratio between these regions is 38.6 (n = 22 cells).

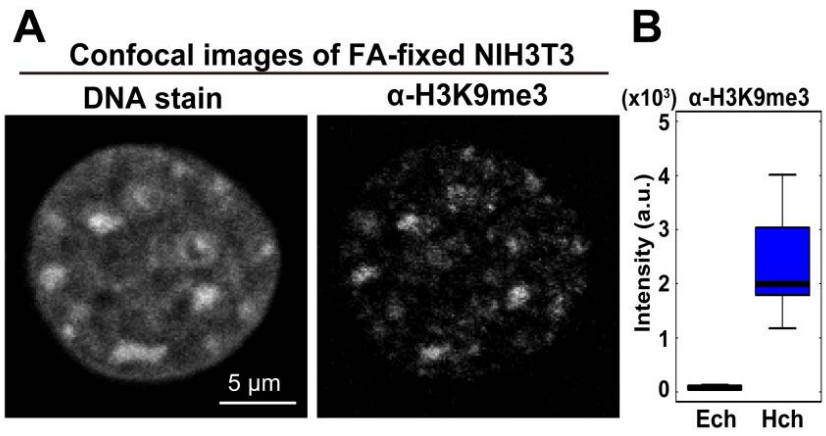

Figure 43. The enrichment of H3K9me3 at pericentric foci.

(A) Confocal images of DNA staining (DAPI) and immunostaining with α-H3K9me3 in a fixed NIH3T3 cell. Consistent with MeCP2-EGFP, the regions surrounding pericentric foci were almost free of α-H3K9me3 signals. Scale bar: 5 μm. (B) The signal intensity quantification of the images in (A). The fluorescence ratio is 32.3 (n = 21 cells).

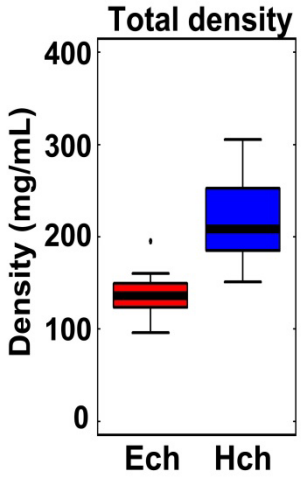

Figure 44. The estimated total densities of pericentric heterochromatin foci (Hch) and surrounding euchromatin (Ech).

Their values were 208 and 136 mg/mL, respectively. The median density ratio between them was 1.53. Ech, n = 13; Hch, n = 26.

Interestingly, the density of pericentric foci was 208 mg/mL, whereas that of the surrounding euchromatin was 136 mg/mL (Figure 44; Table 1). The difference between these two densities (heterochromatin/euchromatin) was only 1.53-fold (Figure 44). To

compare the obtained total density of the pericentric foci with their DNA density, I examined the fluorescence intensity of Hoechst-stained live mouse NIH3T3 cells using confocal laser scanning microscopy (Figure 45, left). In accordance with a previous report (Bancaud et al, 2009), the intensity of DNA staining was 7.5-fold higher than that of the surrounding regions (Figure 46), which was much greater than the total density difference (1.53-fold). Live NIH3T3 cells expressing histone H3.1-EGFP (Figure 45, right) also showed that the intensity of EGFP in the foci was 5.5-fold higher than that of the surrounding regions (Figure 47), thus excluding possible bias resulting from the high affinity of the Hoechst dye to the AT-rich sequences of the foci. Furthermore, this 5.5–7.5-fold density difference is consistent with those estimated from volumes of specific heterochromatin (inactive/repressed) and euchromatin (actively transcribed) regions based on super-resolution imaging, ChIP-seq, and DNA-FISH techniques (Boettiger et al, 2016). Taken together, these results suggest that, although DNA was highly condensed at the pericentric heterochromatin foci, the total density of the regions (including non-nucleosomal materials such as proteins and RNAs) was comparable to that of the surrounding euchromatin regions (Figure 44).

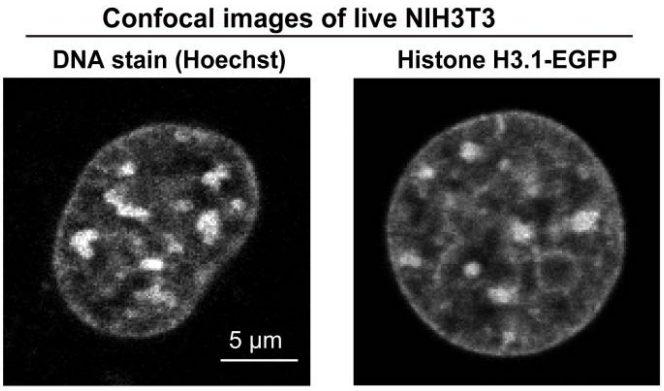

Figure 45. Typical confocal images of Hoechst 33342 and H3.1-EGFP signals in live NIH3T3 cells. Large foci in the nuclei are pericentric heterochromatin foci. Scale bar: 5 μm.

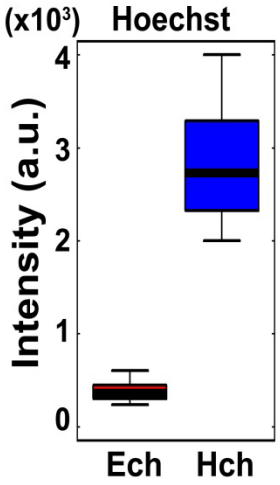

Figure 46. Differences in signal intensity between the heterochromatin (Hch) and surrounding euchromatin (Ech) regions in live NIH3T3 cells analyzed from Hoechst stained images. Signal intensity ratio: 7.5. n = 18.

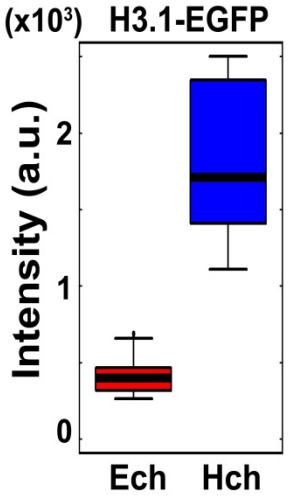

Figure 47. Differences in signal intensity between the heterochromatin (Hch) and surrounding euchromatin (Ech) regions in live NIH3T3 cells analyzed from H3.1-EGFP images. Intensity ratio: 5.5. n = 16.

I also measured the total densities of cytoplasm and nucleoli in live NIH3T3 cells (Figures 34A and 48; Table 1). These cellular features were specifically labeled in live

cells using calcein (Morris, 1990) and EGFP-fibrillarin (Ochs et al, 1985), respectively. The density of cytoplasm (165 mg/mL) was slightly higher than that of the nucleoplasm, except for the pericentric foci. The density of nucleoli (259 mg/mL) was the greatest among the cellular compartments I quantified (Table 1; see also the Discussion). While performing OI-DIC imaging and density estimation on live cells, I found that methanol (MeOH)-fixation and formaldehyde (FA)-fixation increased and decreased the density of heterochromatin foci, respectively (MeOH, 289 mg/mL; FA, 174 mg/mL) (Figure 49; Table 1). This result is consistent with the density of centromeric heterochromatin (165 mg/mL) in FA-fixed human cells measured by the coherent anti-Stokes Raman scattering (CARS)-based system (Pliss et al, 2010). Furthermore, the density of the cytoplasm clearly declined after each treatment (MeOH, 136 mg/mL; FA, 145 mg/mL) (Figure 49; Table 1). These results show that the localization of nuclear and cytoplasmic materials was altered by the fixation processes, indicating that live-cell imaging is critical for proper density estimation.

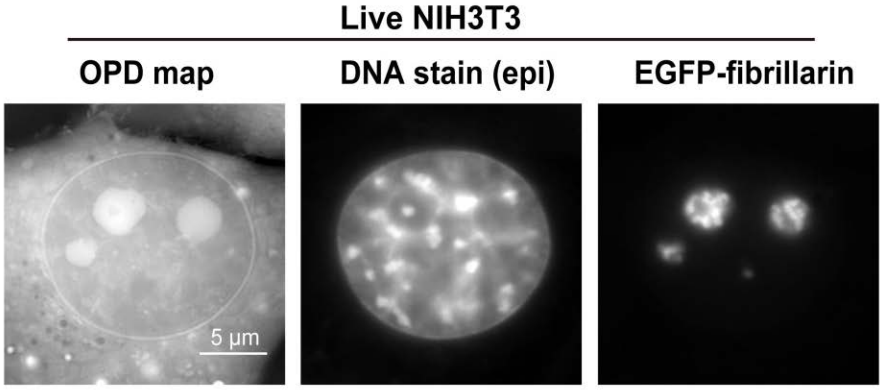

Figure 48. OPD maps (left), DNA staining (center) and EGFP-fibrillarin (right) images of live NIH3T3 cells.
The high-density regions in OPD maps (which co-localized with EGFP-fibrillarin signals, a nucleoli marker) were nucleoli.

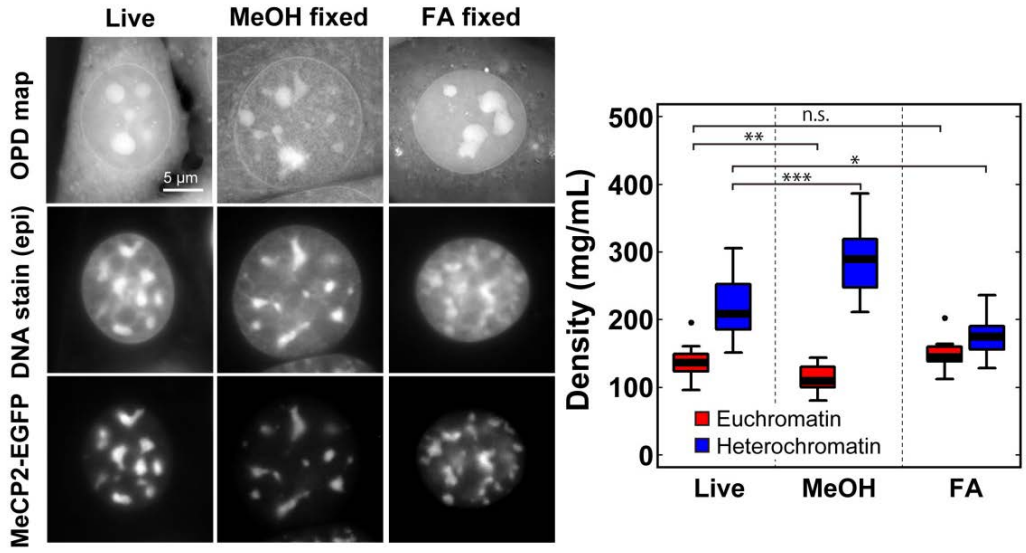

Figure 49. Density changes in cells upon fixation.
(Left) OPD maps (1st row), DNA staining (2nd row) and MeCP2-EGFP (3rd row) images of live NIH3T3 cells with MeOH fixation (center column) and FA fixation (right column). (Right) The densities of euchromatin and pericentric heterochromatin in MeOH- and FA-fixed cells. Under the MeOH fixation condition, n = 10 for euchromatin and n = 20 for heterochromatin. Under the FA fixation condition, n = 8 for euchromatin and n = 16 for heterochromatin. n.s.: not significant; *p < 0.01; **p < 0.001; ***p < 0.0001, Student's *t*-test.

Composition estimation of the pericentric heterochromatin foci in live cells

Given that the difference in DNA density between the foci regions and euchromatin was high (Figures 46 and 47), I was interested in determining why the difference in total density between them was so low (Figure 44). To this end, I estimated the density compositions of the pericentric foci and euchromatin. I first calculated the average density of nucleosomes in a single nucleus based on the total mouse genome size (one nucleosome/200 bp DNA; 2.8 G bp DNA in a haploid mouse cell) and nuclear volume (1,000 μm^3; details in Materials and Methods), and obtained a value of 11.5 mg/mL (Figure 50). If it is assumed that this value is similar to the nucleosome density of the

surrounding euchromatic regions, the density of non-nucleosomal materials (proteins, RNAs) should be 125 mg/mL, because the measured total density of the region is 136 mg/mL (Figure 50). Then, given that the DNA (or nucleosome) density of the heterochromatin foci was 7.5-fold higher than in the surrounding euchromatin regions, I calculated the densities of nucleosomes and non-nucleosomal materials in the heterochromatin foci to be 85.9 and 122 mg/mL, respectively (Figure 50). Interestingly, these simple calculations suggested that the density of non-nucleosomal materials (proteins, RNAs) was comparable between the heterochromatin and surrounding euchromatin (Figure 50), and that the non-nucleosomal contribution was dominant in determining these total densities.

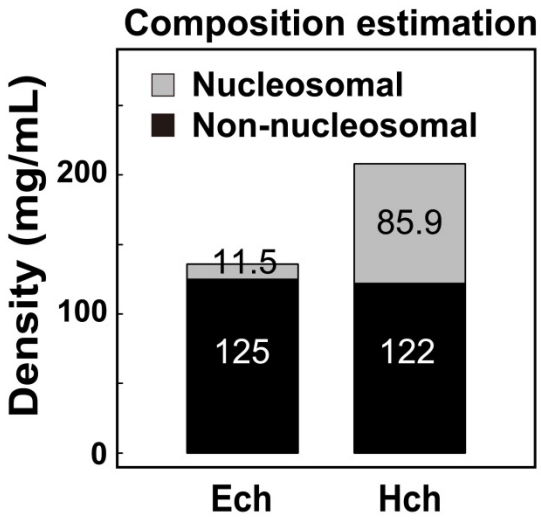

Figure 50. Estimated composition of the pericentric foci and euchromatin in live cells.
Note that non-nucleosomal materials (non-histone proteins, RNAs) were dominant in both chromatin regions. For details, see the Materials and Methods section.

Total density in the inactive X chromosome was only 1.48-fold higher than the surrounding regions

The pericentric foci that I investigated as described above are a model of constitutive

heterochromatin. Therefore, to ascertain the generality of the findings, I examined inactivated human X chromosomes, a classic facultative heterochromatin model (da Rocha & Heard, 2017; Jegu et al, 2017; Nakajima & Sado, 2014; Smeets et al, 2014; Wutz, 2011). To this end, the near-diploid human cell line RPE1 was used. RPE1 cells have brightly stained foci, often attached to the nuclear envelope (Figure 51, right), which are very likely to be condensed inactive X chromosomes with H3K9me3 heterochromatin marks (Nozawa et al, 2013) (Figure 52). I found that the total density of the inactive X chromosome was just 1.48-fold higher than the surrounding regions (137 mg/mL, Figure 53; Table 1), which were almost free of H3K9me3 heterochromatin marks (Figure 52); cytoplasm, nucleoplasm, and nucleoli in live RPE1 cells also had similar densities to NIH3T3 (Figures 51 and 54). These results suggest that the findings in this study can be generalized to different types of heterochromatin.

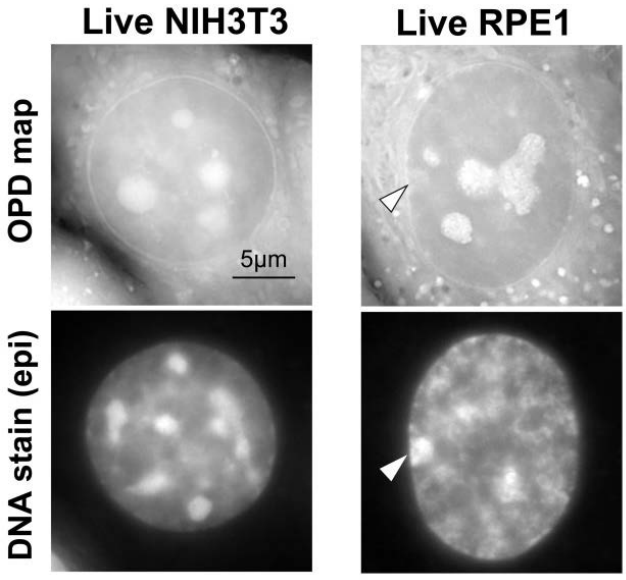

Figure 51. OPD maps (1st row) and DNA staining (2nd row) of live NIH3T3 cells (left) and RPE1 cells (right).
Note that the RPE1 cell has a brightly stained area attached to the nuclear envelope (arrowhead), which is likely to be an inactive X chromosome.

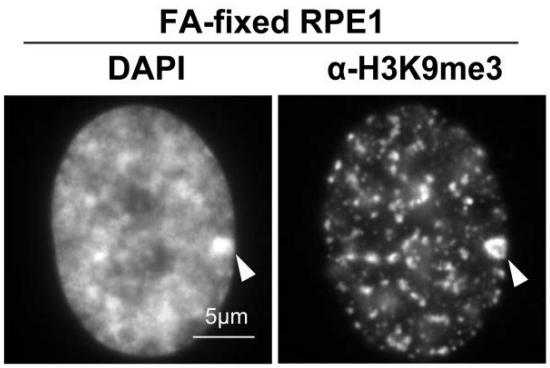

Figure 52. Fluorescence images of DNA staining (DAPI, upper) and α-H3K9me3-immunostaining of FA-fixed RPE1 cells.

Regions surrounding inactive X chromosomes seem to be free of H3K9me3 marks.

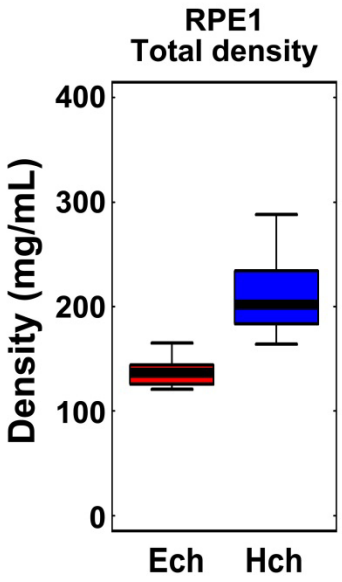

Figure 53. The density of the nucleoplasm (euchromatin) and inactive X chromosome (heterochromatin) in RPE1 cells (density ratio: 1.48, n = 10 for each).

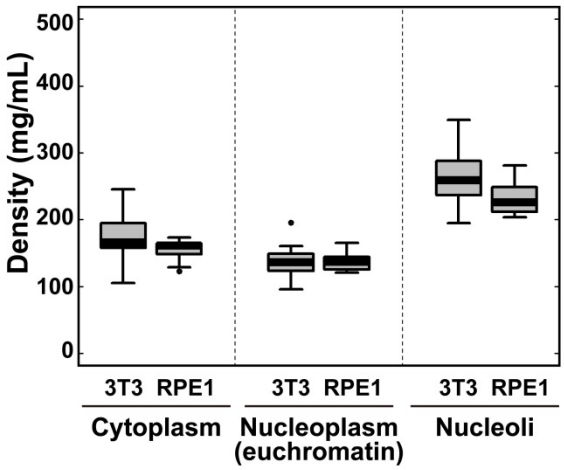

Figure 54. The density of each cellular compartment in NIH3T3 and RPE1 cells.
3T3, n = 13 cells; RPE1, n = 10 cells.

A moderate barrier of access to heterochromatin revealed by Monte Carlo simulation

Although I found that non-nucleosomal materials (proteins, RNAs) were the dominant components of heterochromatin and euchromatin, the biological significance of this finding was not immediately clear. Thus, to investigate the significance of this finding, as collaboration with Dr. Koichi Takahashi and Dr. Kazunari Kaizu at RIKEN, I created a simple computational model of the heterochromatin-euchromatin boundary using Monte Carlo simulation (Metropolis et al, 1953; Morelli & ten Wolde, 2008), which can reproduce the movements of objects such as nucleosomes (Hihara et al, 2012; Maeshima et al, 2015; Nozaki et al, 2013). This type of computational modeling can be used to predict the behavior of proteins under conditions that are either difficult to directly observe by imaging or difficult to generate experimentally (Hibino et al, 2017). I examined the accessibility of the heterochromatin regions by model proteins (tracers) under various conditions (Figure 55).

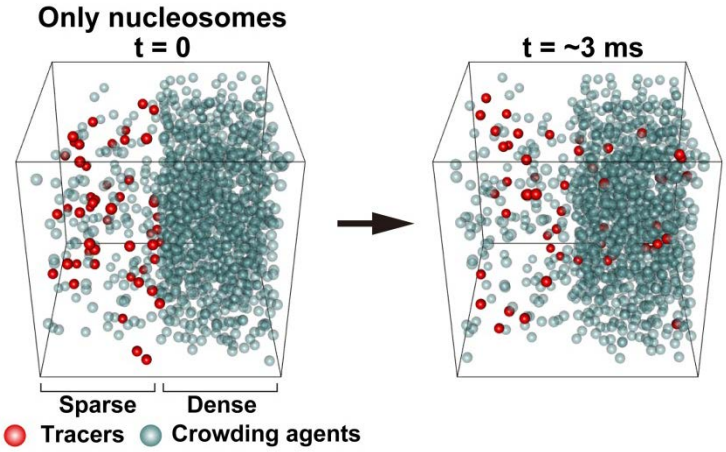

Figure 55. Simulation schemes to study the molecular access to heterochromatin in the "nucleosomes only" situation.

Different numbers of crowding agents (grey balls) were put into the left and right halves of the box at densities corresponding to the nucleosome densities of euchromatin (11.5 mg/mL) and heterochromatin (85.9 mg/mL). Then 50 tracers (red balls) were placed in the left half of the box (left, t = 0), and all balls were randomly moved. Later, some of the tracers (red balls) moved into the heterochromatin region (right, t = ~ 3 ms). I analyzed the fraction of tracers in the dense half and the trajectories of the tracers. To aid in visualization, crowding agents were made transparent.

I defined a cubic space that had two regions, left and right halves (Figure 55). As crowding agents, spheres with 9.6 nm diameters were placed into the left ("sparse") and right ("dense") regions at low and high densities, respectively. For simplicity, the size and weight of nucleosomes were used as representatives of the various crowding agents including nucleosomes, proteins, RNAs, and their complexes. To maintain the density difference between the two regions, movement of the crowding agents was restricted within each region. To investigate accessibility into the dense half, I added spheres with various diameters to the sparse half as tracers and allowed them to move freely within the entire space. To determine whether the density difference created a barrier to the dense region, I measured the fraction of the tracers in the dense half after a period of time.

First, crowding agents were placed into the sparse and dense regions at 11.5 and 85.9 mg/mL, respectively. This represented the nucleosome densities in euchromatin and heterochromatin, respectively, and produced the 7.5-fold density difference between the two regions (Figure 55). Under these conditions, small tracers (5–10 nm in diameter) moved quite freely within the entire space (Figure 56; Table 2), although some suppression of access to the dense region (heterochromatin) by large tracers was observed, presumably due to the excluded volume effect in the dense region.

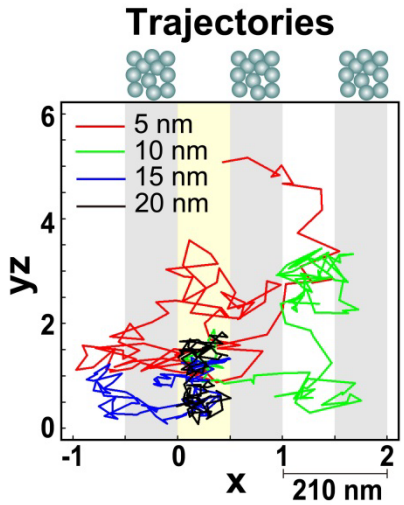

Figure 56. Typical trajectories of the tracers in the simulation corresponding to Figure 55 with periodic boundaries.
The trajectories were two dimensionally projected onto an x-yz plane. yz is a cylindrical coordinate; $yz = (y^2 + z^2)^{1/2}$. The dense regions are shaded in grey, and the starting regions for the tracers are marked with yellow. Tracers with diameters of 5 or 10 nm could easily diffuse into the dense regions.

Next, I added more crowding agents, representing non-nucleosomal materials, to the sparse and dense regions: 136 mg/mL in the sparse region and 208 mg/mL in the dense region (Figure 57). I observed an access suppression effect, particularly for large tracers

10–20 nm in diameter (Figures 58 and 59; Table 2), which is consistent with the *in vivo* situation (Bancaud et al, 2009; Baum et al, 2014; Cremer et al, 2015). This suggested that the dominance of non-nucleosomal materials contributed to the creation of a moderate access barrier for heterochromatin. After adding more crowding agents to the dense region to a total density of 136–340 mg/mL (1.53- to 2.5-fold density difference), the access-barrier effect became more severe (Figure 59). With sphere tracers of 20 nm in diameter, the accessibility to heterochromatin was almost completely inhibited (Figure 59).

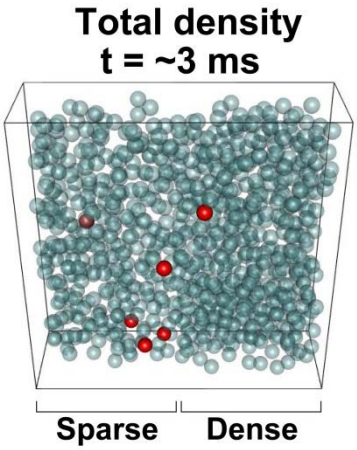

Figure 57. A snapshot of the simulation with additional crowding agents (non-nucleosomal materials): sparse euchromatin (left, 136 mg/mL) and dense heterochromatin (right, 208 mg/mL) regions at t = ~ 3 ms.
To aid in visualization, only part of the simulation space is presented (20% of the entire space, 210 × 210 × 42 nm).

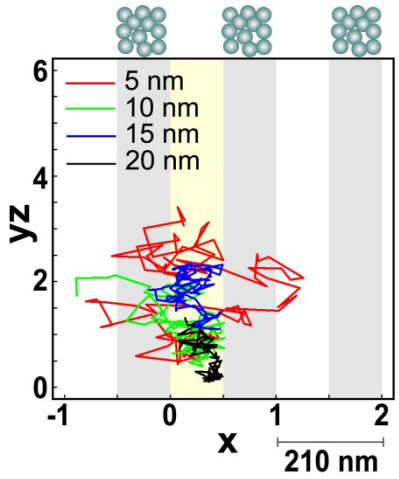

Figure 58. Typical trajectories of the tracers in the simulation corresponding to Figure 57 with periodic boundaries.

Note that the diffusions of tracers were suppressed to a greater degree than in Figure 56.

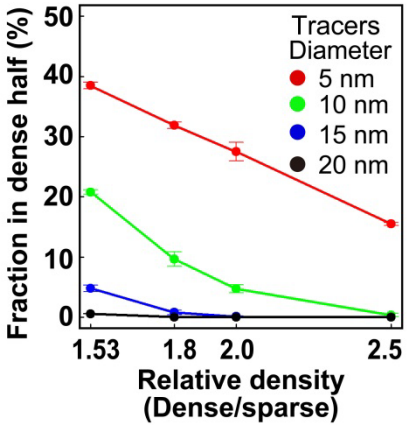

Figure 59. Fraction of tracers localized in the dense region under various density conditions.

For each tracer type (5, 10, 15, and 20 nm diameter), the fraction within the dense half at equilibrium (~ 50 ms) is shown. Note that the 1.53-fold higher density corresponds to the estimated density ratio between heterochromatin and euchromatin in live cells.

2.3. Discussion

To elucidate the physical properties of chromatin, I used a novel OI-DIC imaging method and subsequent computational analysis (Figures 32, 34-37, and 40) to calculate the absolute density of heterochromatin and adjacent euchromatin regions, including nucleosomes and non-nucleosomal materials (e.g. proteins, RNAs) in live cells (Figures 44 and 53). Based on the difference in DNA density between these regions (i.e., a 5.5- to 7.5-fold difference) (Figures 46 and 47), it was expected that heterochromatin would be very dense. Surprisingly, I found that the pericentric foci (208 mg/mL) and inactive X chromosomes (202 mg/mL) were only 1.53- and 1.48-fold denser, respectively, than the surrounding euchromatin (Figures 44 and 53; Table 1). This may be because non-nucleosomal materials were dominant (~120 mg/mL) in both regions (Figure 50). This study provides a novel “live” view of heterochromatin that includes not only densely packed nucleosomes but also non-nucleosomal proteins and RNAs.

The simulation results suggested that nucleosomes alone could not create an efficient barrier of access to heterochromatin regions (Figures 46 and 47) and that the addition of non-nucleosomal materials to both the sparse and dense regions contributed to the formation of a moderate barrier to proteins accessing dense regions (Figures 58 and 59; Table 2). This result is consistent with *in vivo* observations that a small fraction of large fluorescent dextran (~ 500 kDa) can diffuse into pericentric heterochromatin in NIH3T3 cells (Bancaud et al, 2009), see also (Baum et al, 2014; Cremer et al, 2015). This type of moderate barrier, which allows minimal protein access to heterochromatin and makes the regions structurally controllable, may play an important role in heterochromatin functions such as low-level transcription (Saksouk et al, 2015; Trojer & Reinberg, 2007)

and mid-to-late S phase DNA replication (Guenatri et al, 2004; Wu et al, 2006). On the other hand, the nucleoli, whose density was the highest (259 mg/mL) among the cellular components (Figure 48; Table 1), might present a much stronger barrier to protein access and require active transport systems for proteins. Consistently, it has been reported that nucleolar localization signals exist that target proteins to nucleoli (Hatanaka, 1990; Scott et al, 2010).

Besides the access barrier function of non-nucleosomal proteins and RNAs, I suggested that a high concentration (~ 120 mg/mL) of the non-nucleosomal materials generates the macromolecular crowding effect/depletion attraction seen in crowded environments, where 20–30% of the volume is occupied by soluble proteins and other macromolecules (Asakura & Oosawa, 1954; Hancock, 2007; Marenduzzo et al, 2006). I further proposed that this effect plays an important role in local chromatin compaction in the process of heterochromatin formation, as suggested previously (Bancaud et al, 2009; Golov et al, 2015; Walter et al, 2013). Furthermore, since recent studies using super-resolution imaging or the Hi-C technique have revealed that chromatin is organized as domains (Cremer et al, 2017; Dixon et al, 2012; Eagen et al, 2015; Markaki et al, 2010; Nora et al, 2012; Nozaki et al, 2017; Rao et al, 2014; Sexton et al, 2012) with various sizes (~ 100–200 nm), the macromolecular crowding effect caused by high concentrations of non-nucleosomal materials may also contribute to the formation of chromatin domains. Consistent with this notion, hypotonic treatment of live cells, which likely reduces the crowing effect, was shown to decondense the chromatin domain structure (Nozaki et al, 2017).

From a technical perspective, the results in this study confirmed that OI-DIC imaging could achieve a lateral resolution of ~ 300 nm and low OPD noise levels (~ 0.5 nm) at a wavelength of 546 nm. The pericentric heterochromatin (Figures 40-44) and inactive X chromosomes (Figures 51-53) have micron-sized dimensions suitable for examination. On the other hand, because of the resolution limitation, we must bear in mind that the obtained total densities in the euchromatic regions that we measured were the averaged values of the chromatin domains (~ 100–200 nm) and surrounding domain-free regions.

Finally, I would emphasize the importance of live cell studies to understand the biophysical nuclear properties, which govern nuclear functions and both facilitate and constrain the diffusion of protein factors and their complexes. This study sheds new light on the need to consider not only chromatin compaction (DNA density) but also non-nucleosomal materials (proteins, RNAs) as obstacles of a free diffusion. The obtained density information can provide critical physical parameters for comprehensive computational modeling of chromatin and chromosomes (e.g. (Cheng et al, 2015; Ozer et al, 2015; Shinkai et al, 2016)).

2.4. Materials and Methods

OI-DIC imaging system for biological samples

The principal schematic of the OI-DIC microscopy system is shown in Figure 32. The microscope includes a light source with a bandpass filter, crossed linear polarizer and analyzer, phase shifter, condenser and objective lenses, tube lens and CCD camera. To overcome the limitations of conventional DIC imaging, the microscope contains two beam-shearing assemblies (Shribak, 2014). Each assembly consists of two identical DIC prisms and a 90° polarization rotator. Rotating light polarization by the rotators allows the shear directions to be rapidly switched by 90° without mechanically rotating the samples (e.g., live cells) or the prisms. Six raw images were captured using OI-DIC microscopy, with two perpendicular shear directions and three biases ± 0.15λ and 0, where λ is the wavelength. The captured OI-DIC images were processed into OPD images (maps) whose intensity corresponded linearly to the OPD value. Image processing was performed using home-built software (OIDIC.exe). This and other processing algorithms were previously described (Shribak, 2013; Shribak & Inoue, 2006; Shribak et al, 2017).

Mathematical model of OI-DIC microscopy

For convenience of the reader the mathematical principles of OI-DIC technique and one of image processing algorithms were briefly explained. The OI-DIC mathematical model along with several processing algorithms were reported in detail elsewhere (Shribak, 2013; Shribak & Inoue, 2006; Shribak et al, 2017).

The intensity distribution in the DIC image $I(x,y)$ can be described by using a model of interference of two overlapping identical coherent images with optical path difference

OPD(x,y), slightly offset from each other:

$$I(x,y) = \tilde{I}\sin^2\left\{\frac{\pi}{\lambda}\left[\Gamma + \mathbf{d}\cdot\mathbf{G}(x,y)\right]\right\} + I_c(x,y),$$

where $\tilde{I}$ is the initial beam intensity, λ is wavelength, Γ is bias, d is shear vector, G(x,y) is the optical path difference gradient vector, and $I_c(x,y)$ corresponds to an offset of the intensity signal, which caused by the stray light.

The optical path difference gradient vector G(x,y) is the following:

$$\mathbf{G}(x,y) = \left(\frac{d(OPD(x,y))}{dx}, \frac{d(OPD(x,y))}{dy}\right) = \left(\gamma(x,y)\cos\theta(x,y), \gamma(x,y)\sin\theta(x,y)\right),$$

where $\gamma(x,y)$ and $\theta(x,y)$ are optical path difference gradient magnitude and azimuth, respectively.

In order to map the optical path difference gradient vector G(x,y) the OI-DIC microscope varies shear vector d and bias Γ. two sets of raw DIC images is captured at shear directions -45º and +45º with negative, zero and positive biases: $-\Gamma_0$, 0, and $+\Gamma_0$. Typically biases ±0.15λ and 0 are used.

The following group of equations represents these six DIC images:

$$I_{i,j}(x,y) = \tilde{I}\sin^2\left\{\frac{\pi}{\lambda}\left[j\Gamma_0 + \sqrt{2}\,d\,\gamma(x,y)\cos\left(\theta(x,y) - (-1)^i\frac{\pi}{4}\right)\right]\right\} + I_c(x,y),$$

where j = -1, 0, 1, and d is shear amount (magnitude of shear vector).

Initially two terms are computed (i = 1, 2):

$$A_i(x,y) = \frac{I_{i,1}(x,y) - I_{i,-1}(x,y)}{I_{i,1}(x,y) + I_{i,-1}(x,y) - 2I_{i,0}(x,y)}\tan\left(\frac{\pi\Gamma_0}{\lambda}\right).$$

Using the obtained terms we can calculate the quantitative two-dimension distributions of the gradient magnitude and azimuth of optical path difference in the specimen as:

$$\gamma(x,y)=\frac{\lambda}{2\sqrt{2}\,\pi d}\sqrt{\sum_{i=1}^{2}\arctan^2\left[A_i(x,y)\right]},$$

$$\theta(x,y)=\arctan\left(\frac{\arctan A_2(x,y)}{\arctan A_1(x,y)}\right)-\frac{\pi}{4}.$$

The gradient magnitude represents increment of the optical path difference, which is in nanometers, along lateral coordinate, which is also in nanometers. Thus, the gradient magnitude is unitless.

The obtained two-dimension distribution of optical path difference gradient vector G(x,y) is used for computing the optical path difference map *OPD(x,y)*. For this purpose the gradient vector G(x,y) can be presented as a complex number:

$$\mathbf{G}(x,y)=\frac{\partial(OPD(x,y))}{\partial x}+i\frac{\partial\phi(OPD(x,y))}{\partial y}=\gamma(x,y)e^{i\theta(x,y)}, \qquad (1)$$

where real and imaginary parts are X- and Y- components of the gradient vector, respectively.

At first the 2-dimensional Fourier transform is applied to the left and the middle parts of the equation above. Then the resultant integral equation can be solved by partial integration. After using the inverse 2-dimensional Fourier transform the following formula is obtained for computation of the optical path difference *OPD(x,y)*:

$$OPD(x,y)=F^{-1}\left[\frac{F\left[\mathbf{G}(x,y)\right]}{i(\omega_x+i\omega_y)}\right],$$

where ω_x and ω_y are spatial angular frequencies.

Taking into account the right part of equation (1), finally we get formula for computing the OPD:

$$OPD(x,y)=F^{-1}\left[\frac{F\left[\gamma(x,y)e^{i\theta(x,y)}\right]}{i(\omega_x+i\omega_y)}\right].$$

Then a computed two-dimensional distribution of the optical path difference is transformed into quantitative 8-bit greyscale image (map), where the image brightness is linearly proportional to value of the OPD and the maximum grey level of 255 corresponds to the chosen OPD ceiling.

Density estimation of cellular contents

To obtain calibration curves of the RIs of proteins and nucleic acids (Figure 37), bovine serum albumin (BSA, Sigma A-9418), and salmon sperm DNA (Fisher Scientific, BP-2514) were dissolved in cell culture medium at concentrations of 0–200 and 0–30 mg/mL, respectively. The RIs of the prepared standard solutions were measured with a refractometer, Abbé-3L (BAUSCH & LOMB). The measured RIs and solution densities were plotted and fitted with linear functions to obtain calibration curves.

I estimated intracellular density distribution from obtained OPD maps using the following two steps (Figure 33). First, I calculated the RI from the OPD. Because the OPD is proportional to the thickness of a sample and the difference in RI between the sample and the surrounding solution, as shown in Figure 33, I calculated the RI of samples based on the RI of the surrounding solution and sample thickness. Second, I obtained the dry mass density ("density" for short) of the sample from its RI, because the RI of a sample is proportional to its density. For proteins and nucleic acids, which are the dominant materials in mammalian cells (> 60% of dry mass) (Alberts et al, 2007), my calibration curves (Figure 37; see above) of RI versus dry mass density using BSA and salmon sperm DNA showed that both were well fitted to linear functions and were almost identical ($RI = 1.3375 + 1.4 \times 10^{-4} \times C$, where C is dry mass density).

Therefore, dry mass density in live cells, which consists mainly of proteins and nucleic acids, was calculated from their RI using a single calibration curve (Figure 37). To estimate the densities of the total cell contents, I measured the average thickness of the cytoplasm and nucleus in each cell line (Figure 34). The pericentric foci were assumed to be spherical (Figure 35). To obtain the RI of cytoplasm (RI_{cy}), I used the RI of the surrounding culture medium (RI_{med}, 1.3375) (Figure 36). For the RIs of the nucleus and the pericentric foci, I used my calculated values of RI_{cy} and RI_{nuc}, respectively (Figure 36). These estimates were created using ImageJ software.

EGFP-MeCP2 construction

A plasmid containing MeCP2-EGFP was kindly provided by Professor Cardoso (Brero et al, 2005). The moiety of MeCP2-EGFP was cut by *Xho*I and *Xba*I enzymes and blunted. The blunted fragment was inserted into the *Eco*RV site of the pEF5/FRT/VS-DEST Gateway Vector (Invitrogen) to generate pEF5-MeCP2-EGFP-FRT.

EGFP-mH3.1p-H3.1 construction

A mouse histone H3.1 promoter (~840 bp)-H3.1 fragment was amplified from mouse embryonic stem (ES) cell genomic DNA by PCR using the following primer set: 5'- AAACATTACGAATCACCAAAGGCTCTTTTCAGAGCCACTC -3' and 5'- AGCCCTCTCCCCGCGGATGCGGCGGGCCAGCTGGATGTCC -3'. The amplified fragment was cloned into an EGFP vector to obtain pmH3.1p-H3.1-EGFP. Then, two more insert sequences were prepared. One was the H3.1promoter-H3.1-EGFP amplified from the pmH3.1p-H3.1-EGFP vector using the following primer set:

5’- TAGGCTTTTGCAAAAAGCTTAAACATTACGAATCACCAAA -3’ and 5’- TTACTTGTACAGCTCGTCCATGCCGAGAGT -3’. The other was the 3’ untranslated region of H3.1 (~ 500 bp) amplified from the mouse ES genome using the primer pair: 5’- TGGACGAGCTGTACAAGTAAAGTTCGTCTTTCTGTGTTTTTCAAAGGCTC -3’ and 5’- GCTTGACGGGGAAAGAAGCTGCTGGTTGTAGCACTTTGGGTTGTTCTGGG -3’.

For backbone vector preparation, the region from the EF1α-promoter to the BGH polyadenylation signal sequence was removed from pEF5/V5-FRT Gateway (Invitrogen) to create the pFRT-Hygromycin vector. The pFRT-Hygromycin vector, H3.1promoter-H3.1-EGFP sequence, and 3’ untranslated region sequence were ligated by SLIC (Li & Elledge, 2007) to prepare the pmH3.1p-H3.1-EGFP-3’UTR-FRT plasmid. In addition, upstream of the H3.1 promoter, an insulator fragment (tandem cHS4 kindly provided by Dr. Felsenfeld) was inserted to obtain pIx2-mH3.1p-H3.1-EGFP-3’UTR-FRT.

EGFP-fibrillarin construction

To clone the fibrillarin gene, total RNA was isolated from NIH3T3 cells using the RNeasy Mini Kit (Qiagen), and first-strand cDNA was synthesized using the SuperScript III First-Strand Synthesis System (Thermo) with oligo(dT). The coding region of fibrillarin was amplified from the first-strand cDNA using the following primer pair: 5’- GGGGTACCATGAAGCCAGGTTTCAGCCC -3’ and 5’- GCGGGATCCTCAGTTCTTCACCTTGGGAG -3’. The amplified fragment was

digested with *Kpn*I and *Bam*HI, and ligated into *Kpn*I/*Bam*HI-digested pEGFP-C1 (Clontech, Palo Alto, CA). EGFP-fibrillarin fragments were excised, blunt-ended using T4 DNA polymerase (Takara, Japan), and inserted into *Eco*RV-precut pEF1-FRT to generate pEF1-EGFP-fibrillarin-FRT.

Cell culture and stable cell lines

RPE1, a human cell line, and NIH3T3, a mouse cell line, were used. All of the cell lines were maintained in Dulbecco's Modified Eagle's Medium (Lonza) supplemented with 10% (v/v) fetal bovine serum and 0.584 g/L L-glutamine (Sigma) at 37°C with 5% CO_2 in air in a humidified incubator. To establish NIH3T3 cells expressing MeCP2-EGFP, EGFP-fibrillarin, or H3.1-EGFP, the Flp-In system (Invitrogen) was used as previously described (Hihara et al, 2012; Maeshima et al, 2010b).

Live-cell OI-DIC microscopy imaging

Cells were seeded on 24 mm × 24 mm square glass coverslips coated with poly D-lysine (Sigma) and cultured for 1–2 days. Then 30 min before imaging, 500 ng/mL Hoechst 33342 was added into the media and incubated further. The cells were mounted on a glass slide with a thin silicone spacer. I observed the mounted cells by OI-DIC and fluorescence imaging.

OI-DIC imaging of glass rods

A small number of glass rods 4 μm in diameter were suspended in two types of mineral oil with refractive indices of 1.54 and 1.58. Approximately 2 μL of the suspended solution was sandwiched between a glass slide and a coverslip, and then sealed with nail

polish. The glass rods in the mineral oil were analyzed by OI-DIC microscopy using the same procedure as the live cell imaging.

Fixation

For formaldehyde fixation, cells on the square glass coverslips were washed once with phosphate-buffered saline (PBS), and then fixed in 4% formaldehyde at room temperature for 15 min. The fixed cells were washed with 10 mM Hepes-KOH pH 7.5, 100 mM KCl, and 1 mM $MgCl_2$ (HMK) (Maeshima et al, 2006) and permeabilized with 0.5% Triton X-100 in HMK at room temperature for 5 min. The treated cells were washed with HMK, stained with 500 ng/mL Hoechst 33342 in HMK at room temperature for 10 min, and then washed again with HMK. For MeOH fixation, cells on coverslips were fixed in ice-cold MeOH at -20°C for 30 min. Then the fixed cells were washed with HMK at room temperature for 15 min, stained with 500 ng/mL Hoechst 33342 in HMK for 10 min, and washed again with HMK. Finally, the cells were mounted on a glass slide and observed as described above.

Immunostaining of histone H3K9me3

Immunostaining was performed as previously described (Hihara et al, 2012; Maeshima et al, 2010b). Cells were fixed in 2% formaldehyde (Wako) and permeabilized with TX-100. The primary and secondary antibodies were mouse anti-H3K9me3 (a generous gift from Professor Hiroshi Kimura) and Alexa-Fluor-594-conjugated goat anti-mouse IgG (Invitrogen) used at dilutions of 1:500 and 1:1,000, respectively. Then DAPI (500 ng/mL) was added to the cells for 5 min, followed by washing with PBS. Images were obtained using a DeltaVision microscopy imaging system (Applied Precision) or a

FLUOVIEW FV1000 confocal laser scanning microscope (OLYMPUS).

Measurements of cell thicknesses

Live RPE1 and NIH3T3 cells were seeded on 35 mm glass-bottom dishes. To fluorescently label DNA and cytoplasm, cells were incubated in culture medium containing 0.5 µg/mL Hoechst 33342 (Dojindo) and 5 µg/mL Calcein-AM (Dojindo) for 30 min. After washing out excess fluorescent dye, the stained cells were observed under an OLYMPUS FLUOVIEW FV1000 confocal laser scanning microscope equipped with a 60×/1.2 NA water objective. Hoechst 33342 and Calcein-AM fluorescent signals were acquired as 3D image stacks (500 nm × 32 sections). The thicknesses of three regions (nucleus, cytoplasm, entire cell, see Figure 34) were measured in each cell line from the acquired stack images by ImageJ software.

Measurement of nuclear volume of live cells

Image stacks of live NIH3T3 and RPE1 cells acquired to measure cell thickness (described above) were used. The images were converted into binary images by auto thresholding in ImageJ software. Then the volumes of binary image stacks were analyzed using the 3D Objects Counter ImageJ plugin (Bolte & Cordelieres, 2006) (Figure 60).

Quantification of fluorescence from Hoechst-stained DNA, MeCP2-EGFP, and α-H3K9me3

Image stacks of live or immunostained NIH3T3 cells (described above) were used. The middle sections of Hoechst-stained nuclei were selected from the z-stack images. The

highest intensity of a focal plane of heterochromatin and the mean intensity of the surrounding low-intensity region in a nucleus were taken as the intensities of heterochromatin and the surrounding euchromatin. These values were adjusted to account for the background intensity.

Composition estimation of euchromatin and heterochromatin in live cells

The genome size of diploid mouse cells is 5.6×10^9 bp. Because 1 pg of DNA is 978×10^6 bp (978×10^6 bp/pg), the mass of the whole mouse genome is 5.73 pg. If it is assumed that nucleosomes (core histones + DNA) form every 200 bp of the genome and that the mass ratio of core histones to DNA is around 1:1, the mass of the nucleosomes in a mouse nucleus is 11.5 pg (5.73 × 2). The average mouse nuclear volume was calculated to be ~ 1,000 μm^3 (described above) (Figure 60), and the density of nucleosomes in mouse euchromatin was calculated to be 11.5 mg/mL. Further estimates are described in the Results section.

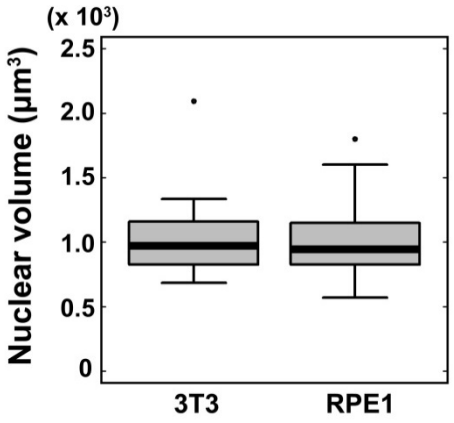

Figure 60. Nuclear volume measurements of the two cell lines.
NIH3T3, n = 25 cells; RPE1, n = 23 cells

Monte Carlo simulation

Monte Carlo simulation is a computational algorithm that performs a numerical integration by making a random movement and evaluating whether the movement is acceptable based on the change in potential energy (Hibino et al, 2017). All of the molecules in the simulations were treated as hard spherical bodies. I employed a Metropolis Monte Carlo method without long-range potential or hydrodynamic interactions to determine the diffusive motion of molecules (Morelli & ten Wolde, 2008). The diameters and diffusion coefficients (*D*s) of the crowding agents used in the simulations were 9.6 nm and 9 $\mu m^2 s^{-1}$, respectively, which are comparable to those of a single nucleosome molecule. The *D*s of tracers (spheres with diameters of 5, 10, 15, and 20 nm) were 18, 9, 6, and 4.5 $\mu m^2 s^{-1}$, respectively. These *D*s were determined by the Stokes–Einstein relationship based on parameters from the EGFP monomer, the diameter and *D* of which were 3.8 nm and 23.5 $\mu m^2 s^{-1}$, respectively (Hihara et al, 2012). Simulations were conducted in a 210 nm cubic box with two compartments (left and right halves). For the “nucleosomes only” scenario, which corresponds to 11.5 mg/mL (euchromatin) and 85.9 mg/mL (heterochromatin), 134 and 968 copies of 9.6 nm spheres (crowding agents) were randomly placed in the left and right halves of the box, respectively. These crowding agents mimicked nucleosomes displaced less than 5 nm from their initial positions at t = 0 s (the “dog on a leash” model; see also (Hihara et al, 2012; Maeshima et al, 2015)). Then 50 tracers that could diffuse freely were placed in the left (euchromatin) region. The motion of the molecules was iteratively simulated following previously described procedures (Hihara et al, 2012; Maeshima et al, 2015). For the second simulation (nucleosomes + non-nucleosomal materials), 1,578 and 1,578–3,945 9.6 nm spheres (crowding agents) were randomly placed in the left and

right regions of the box, respectively, to represent euchromatin and heterochromatin (1.53–2.5-fold density differences). To represent nucleosomes, 134 and 968 9.6 nm spheres were randomly placed in the left and right regions, with their behavior following the “dog on a leash” model. The rest of the spheres moved freely only in each half, to represent diffusing proteins and RNAs. Then 50 tracers were placed in the left (euchromatin) region. Although the simulation process was similar to the first simulation, the movements of crowding agents were restricted within their regions to keep the density of each region constant. Results were obtained by averaging 150 samples from three independent trials. The simulation time step, Δt, was 10 ns.

Statistical analyses

All of the statistical analyses were performed using the two-tailed Student’s *t*-test. P values less than 0.05 were considered statistically significant.

Acknowledgements

These researches would not have been possible without great help from many people. At first I would like to express my deepest gratitude to my supervisor Prof. Kazuhiro Maeshima for his excellent guidance, kind encouragement, and providing me with original philosophy for research. His attitude for science inspires my feeling of respect.

For the help for the research described in Chapter 1, I would like to thank many people: Dr. Seiji Komeda (Suzuka University of Medical Science) and Ms. Masako Uemura (Suzuka University of Medical Science) for synthesis of 5-H-Y and analysis of DNA-Pt adducts; Prof. Kazuto Yamauchi (Osaka University), Dr. Satoshi Matsuyama (Osaka University), Dr. Mari Shimura (National Center for Global Health and Medicine) and Dr. Akihiro Matsunaga (National Center for Global Health and Medicine) for SXFM analysis; Mr. Yutaka Iida (Toray Research Center, Inc.) for ICP-MS analysis; Prof. Jeffrey C. Hansen (Colorado State University) and Mr. Ryan Rogge (Colorado State University) for analytical ultracentrifuge analysis; Prof. Yuko Yoshikawa (Ritsumeikan University) for some essential advices in the study; Prof. Masato T. Kanemaki (National Institute of Genetics) and Dr. Kohei Nishimura (National Institute of Genetics) for providing some materials and experimental methods for me; Dr. Hideaki Takata (Osaka University) for helping several experiments; Prof. Minoru Takata (Kyoto University) for providing FANCD2-, FANCC-, and FANCL-KO DT40 cells; Prof. Takehiko Kobayashi (The University of Tokyo) for helpful discussions and support.

I would also like to thank many other people for the help for the research described in

Chapter 2: Dr. Michael Shribak (Marine Biological Laboratory) for developing the OI-DIC microscope and giving me a chance to perform experiments with the microscope in his laboratory; Dr. Tomomi Tani (Marine Biological Laboratory) for helping me to establish the method of density calculations; Dr. Koichi Takahashi (RIKEN) and Dr. Kazunari Kaizu (RIKEN) for helping me to perform Monte Carlo simulations; Prof. M. Cristina Cardoso (Technische Universität Darmstadt), Prof. Hiroshi Kimura (Tokyo Institute of Technology), and Prof. Gary Felsenfeld (National Institutes of Health) for providing research materials; Prof. Jan Ellenberg (EMBL) and Dr. Aurélien Bancaud (CNRS) for helpful suggestions; Prof. Thomas Cremer (Ludwig Maximilians-Universität) and Dr. Kuniaki Saito (National Institute of Genetics) for advice and discussion on chromatin organization.

Through my Ph.D. course, my committee members, Prof. Hiroyuki Araki, Prof. Hironori Niki, Prof. Ituro Inoue, and Prof. Masato T. Kanemaki in National Institute of Genetics/SOKENDAI, and Prof. Kenichi Yoshikawa in Doshisha University, always gave me helpful advices and supports. And Dr. Yasushi Hiromi (National Institute of Genetics), Dr. Ichiro Hiratani (RIKEN), and Mitsuhiko Kurusu (National Institute of Genetics) kindly made meaningful discussions on both of my studies. I would like to thank them very much.

I would also like to thank the members of Maeshima laboratory in National Institute of Genetics/SOKENDAI, Assistant Prof. Satoru Ide, Assistant Prof. Kayo Hibino, Dr. Tadasu Nozaki, Ms. Sachiko Tamura, Mr. Ryosuke Nagashima, Ms. Asuka Sasaki, Ms. Mai Tambo, Mr. Tomohiro Yamaguchi, Ms. Kaeko Nakaguchi, and Ms. Hiroko Ochi for helpful discussions, technical assistances, and kind encouragements.

In addition, I would like to thank Prof. Kazuki Saito and members in his laboratory in

Chiba University for giving me a chance to move to Maeshima Laboratory when I was an undergraduate student.

Finally, I would like to thank my family and relatives, especially my parents Osamu and Chiemi and my sister Megumi for their continuous support and encouragement through my life.

The studies in this thesis were supported by Japan Science and Technology Agency (JST) CREST, Japan Society for the Promotion of Science (JSPS), Ministry of Education, Culture, Sports, Science and Technology (MEXT), and the SOKENDAI Short-Stay Study Abroad Program in fiscal year 2015. Computations were partially performed on the National Institute of Genetics (NIG) supercomputer.

References

Alberts B, Johnson A, Lewis J, Raff M, Roberts K, Walter P (2007) *Molecular Biology of the Cell, Fifth Edition*

Albiez H, Cremer M, Tiberi C, Vecchio L, Schermelleh L, Dittrich S, Kupper K, Joffe B, Thormeyer T, von Hase J, Yang S, Rohr K, Leonhardt H, Solovei I, Cremer C, Fakan S, Cremer T (2006) Chromatin domains and the interchromatin compartment form structurally defined and functionally interacting nuclear networks. *Chromosome Res* **14**(7)**:** 707-733

Allen RD, David GB, Nomarski G (1969) The zeiss-Nomarski differential interference equipment for transmitted-light microscopy. *Z Wiss Mikrosk* **69**(4)**:** 193-221

Allis CD, Jenuwein T (2016) The molecular hallmarks of epigenetic control. *Nat Rev Genet* **17**(8)**:** 487-500

Asakura S, Oosawa F (1954) On interaction between two bodies immersed in a solution of macromolecules. *J Chem Phys* **22:** 1255-1256

Bancaud A, Huet S, Daigle N, Mozziconacci J, Beaudouin J, Ellenberg J (2009) Molecular crowding affects diffusion and binding of nuclear proteins in heterochromatin and reveals the fractal organization of chromatin. *Embo J* **28**(24)**:** 3785-3798

Baum M, Erdel F, Wachsmuth M, Rippe K (2014) Retrieving the intracellular topology from multi-scale protein mobility mapping in living cells. *Nat Commun* **5**(4494)**:** 4494

Boettiger AN, Bintu B, Moffitt JR, Wang S, Beliveau BJ, Fudenberg G, Imakaev M, Mirny LA, Wu CT, Zhuang X (2016) Super-resolution imaging reveals distinct chromatin folding for different epigenetic states. *Nature* **529**(7586)**:** 418-422

Bolte S, Cordelieres FP (2006) A guided tour into subcellular colocalization analysis in

light microscopy. *J Microsc* **224**(Pt 3)**:** 213-232

Brero A, Easwaran HP, Nowak D, Grunewald I, Cremer T, Leonhardt H, Cardoso MC (2005) Methyl CpG-binding proteins induce large-scale chromatin reorganization during terminal differentiation. *J Cell Biol* **169**(5)**:** 733-743

Brown SW (1966) Heterochromatin. *Science* **151**(3709)**:** 417-425

Buerstedde JM, Takeda S (1991) Increased ratio of targeted to random integration after transfection of chicken B cell lines. *Cell* **67**(1)**:** 179-188

Chen C, Lim HH, Shi J, Tamura S, Maeshima K, Surana U, Gan L (2016) Budding yeast chromatin is dispersed in a crowded nucleoplasm in vivo. *Mol Biol Cell* **27**(21)**:** 3357-3368

Chen D, Dundr M, Wang C, Leung A, Lamond A, Misteli T, Huang S (2005) Condensed mitotic chromatin is accessible to transcription factors and chromatin structural proteins. *J Cell Biol* **168**(1)**:** 41-54

Cheng TM, Heeger S, Chaleil RA, Matthews N, Stewart A, Wright J, Lim C, Bates PA, Uhlmann F (2015) A simple biophysical model emulates budding yeast chromosome condensation. *Elife* **4:** e05565

Cremer M, Schmid VJ, Kraus F, Markaki Y, Hellmann I, Maiser A, Leonhardt H, John S, Stamatoyannopoulos J, Cremer T (2017) Initial high-resolution microscopic mapping of active and inactive regulatory sequences proves non-random 3D arrangements in chromatin domain clusters. *Epigenetics Chromatin* **10**(1)**:** 39

Cremer T, Cremer M, Hubner B, Strickfaden H, Smeets D, Popken J, Sterr M, Markaki Y, Rippe K, Cremer C (2015) The 4D nucleome: Evidence for a dynamic nuclear landscape based on co-aligned active and inactive nuclear compartments. *FEBS Lett* **589**(20 Pt A)**:** 2931-2943

da Rocha ST, Heard E (2017) Novel players in X inactivation: insights into Xist-mediated gene silencing and chromosome conformation. *Nat Struct Mol Biol* **24**(3)**:** 197-204

Davey GE, Davey CA (2008) Chromatin - a new, old drug target? *Chem Biol Drug Des* **72**(3)**:** 165-170

Deans AJ, West SC (2011) DNA interstrand crosslink repair and cancer. *Nat Rev Cancer* **11**(7)**:** 467-480

Dekker J, Heard E (2015) Structural and functional diversity of Topologically Associating Domains. *FEBS Lett* **589**(20 Pt A)**:** 2877-2884

Demeler B (2005) UltraScan: a comprehensive data analysis software package for analytical ultracentrifugation experiments. *Modern analytical ultracentrifugation: techniques and methods***:** 210-229

Dixon JR, Selvaraj S, Yue F, Kim A, Li Y, Shen Y, Hu M, Liu JS, Ren B (2012) Topological domains in mammalian genomes identified by analysis of chromatin interactions. *Nature* **485**(7398)**:** 376-380

Eagen KP, Hartl TA, Kornberg RD (2015) Stable Chromosome Condensation Revealed by Chromosome Conformation Capture. *Cell* **163**(4)**:** 934-946

Fanconi G (1967) Familial constitutional panmyelocytopathy, Fanconi's anemia (F.A.). I. Clinical aspects. *Semin Hematol* **4**(3)**:** 233-240

Fujikane T, Shimizu T, Tsuji T, Ishida S, Ohsaki Y, Onodera S (1989) Flow cytometric analysis of the kinetic effects of cisplatin on lung cancer cells. *Cytometry* **10**(6)**:** 788-795

Fussner E, Ching RW, Bazett-Jones DP (2011) Living without 30nm chromatin fibers. *Trends Biochem Sci* **36**(1)**:** 1-6

Fussner E, Strauss M, Djuric U, Li R, Ahmed K, Hart M, Ellis J, Bazett-Jones DP (2012) Open and closed domains in the mouse genome are configured as 10-nm chromatin fibres. *EMBO Rep* **13**(11)**:** 992-996

Golov AK, Gavrilov AA, Razin SV (2015) The Role of Crowding Forces in Juxtaposing

beta-Globin Gene Domain Remote Regulatory Elements in Mouse Erythroid Cells. *PLoS One* **10**(10)**:** e0139855

Grewal SI, Jia S (2007) Heterochromatin revisited. *Nat Rev Genet* **8**(1)**:** 35-46

Guenatri M, Bailly D, Maison C, Almouzni G (2004) Mouse centric and pericentric satellite repeats form distinct functional heterochromatin. *J Cell Biol* **166**(4)**:** 493-505

Hancock R (2007) Packing of the polynucleosome chain in interphase chromosomes: evidence for a contribution of crowding and entropic forces. *Semin Cell Dev Biol* **18**(5)**:** 668-675

Hansen JC (2002) Conformational dynamics of the chromatin fiber in solution: determinants, mechanisms, and functions. *Annu Rev Biophys Biomol Struct* **31:** 361-392

Hansen JC, Ausio J, Stanik VH, van Holde KE (1989) Homogeneous reconstituted oligonucleosomes, evidence for salt-dependent folding in the absence of histone H1. *Biochemistry* **28**(23)**:** 9129-9136

Hansen JC, Lohr D (1993) Assembly and structural properties of subsaturated chromatin arrays. *J Biol Chem* **268**(8)**:** 5840-5848

Hatanaka M (1990) Discovery of the nucleolar targeting signal. *Bioessays* **12**(3)**:** 143-148

Heitz E (1928) Das heterochromatin der moose. I *Jahrb wiss Bot* **69:** 762-**818**

Hibino K, Kaizu K, Takahashi K, Maeshima K (2017) Combination approach of live-cell imaging and computational modeling toward further comprehensive understanding genome, chromatin and epigenetics. In *Epigenetics and Systems Biology*, Ringrose L (ed), 1st edition edn, 11, pp 225-238. Academic Press

Hihara S, Pack CG, Kaizu K, Tani T, Hanafusa T, Nozaki T, Takemoto S, Yoshimi T, Yokota H, Imamoto N, Sako Y, Kinjo M, Takahashi K, Nagai T, Maeshima K (2012) Local nucleosome dynamics facilitate chromatin accessibility in living mammalian cells. *Cell Rep* **2**(6)**:** 1645-1656

Hirano S, Yamamoto K, Ishiai M, Yamazoe M, Seki M, Matsushita N, Ohzeki M, Yamashita YM, Arakawa H, Buerstedde JM, Enomoto T, Takeda S, Thompson LH, Takata M (2005) Functional relationships of FANCC to homologous recombination, translesion synthesis, and BLM. *Embo J* **24**(2)**:** 418-427

Hsieh TH, Weiner A, Lajoie B, Dekker J, Friedman N, Rando OJ (2015) Mapping Nucleosome Resolution Chromosome Folding in Yeast by Micro-C. *Cell* **162**(1)**:** 108-119

Inoué S, Spring K (1997) *Video Microscopy*, 2nd edn. New York: Plenum Press.

Jamieson ER, Lippard SJ (1999) Structure, Recognition, and Processing of Cisplatin-DNA Adducts. *Chem Rev* **99**(9)**:** 2467-2498

Jegu T, Aeby E, Lee JT (2017) The X chromosome in space. *Nat Rev Genet* **18**(6)**:** 377-389

Joti Y, Hikima T, Nishino Y, Kamada F, Hihara S, Takata H, Ishikawa T, Maeshima K (2012) Chromosomes without a 30-nm chromatin fiber. *Nucleus* **3:** 404-410

Kim H, D'Andrea AD (2012) Regulation of DNA cross-link repair by the Fanconi anemia/BRCA pathway. *Genes Dev* **26**(13)**:** 1393-1408

Kirkpatrick P, Baez AV (1948) Formation of optical images by X-rays. *J Opt Soc Am* **38**(9)**:** 766-774

Kitao H, Nanda I, Sugino RP, Kinomura A, Yamazoe M, Arakawa H, Schmid M, Innan H, Hiom K, Takata M (2011) FancJ/Brip1 helicase protects against genomic losses and gains in vertebrate cells. *Genes Cells* **16**(6)**:** 714-727

Kociba RJ, Sleight SD, Rosenberg B (1970) Inhibition of Dunning asc itic leukemia and Walker 256 carcinosarcoma with cis-diamminedichloroplatinum (NSC-119875). *Cancer Chemother Rep* **54**(5)**:** 325-328

Komeda S (2011) Unique platinum-DNA interactions may lead to more effective

platinum-based antitumor drugs. *Metallomics* **3**(7)**:** 650-655

Komeda S, Lin YL, Chikuma M (2011) A tetrazolato-bridged dinuclear platinum(II) complex exhibits markedly high in vivo antitumor activity against pancreatic cancer. *ChemMedChem* **6**(6)**:** 987-990

Komeda S, Lutz M, Spek AL, Chikuma M, Reedijk J (2000) New antitumor-active azole-bridged dinuclear platinum(II) complexes: synthesis, characterization, crystal structures, and cytotoxic studies. *Inorg Chem* **39**(19)**:** 4230-4236

Komeda S, Takayama H, Suzuki T, Odani A, Yamori T, Chikuma M (2013) Synthesis of antitumor azolato-bridged dinuclear platinum(ii) complexes with in vivo antitumor efficacy and unique in vitro cytotoxicity profiles. *Metallomics* **5**(5)**:** 461-468

Li MZ, Elledge SJ (2007) Harnessing homologous recombination in vitro to generate recombinant DNA via SLIC. *Nat Methods* **4**(3)**:** 251-256

Lowary PT, Widom J (1998) New DNA sequence rules for high affinity binding to histone octamer and sequence-directed nucleosome positioning. *J Mol Biol* **276**(1)**:** 19-42

Luger K, Mader AW, Richmond RK, Sargent DF, Richmond TJ (1997) Crystal structure of the nucleosome core particle at 2.8 A resolution. *Nature* **389**(6648)**:** 251-260

Maeshima K, Hihara S, Eltsov M (2010a) Chromatin structure: does the 30-nm fibre exist in vivo? *Curr Opin Cell Biol* **22**(3)**:** 291-297

Maeshima K, Iino H, Hihara S, Funakoshi T, Watanabe A, Nishimura M, Nakatomi R, Yahata K, Imamoto F, Hashikawa T, Yokota H, Imamoto N (2010b) Nuclear pore formation but not nuclear growth is governed by cyclin-dependent kinases (Cdks) during interphase. *Nat Struct Mol Biol* **17**(9)**:** 1065-1071

Maeshima K, Imai R, Tamura S, Nozaki T (2014) Chromatin as dynamic 10-nm fibers. *Chromosoma* **123:** 225-237

Maeshima K, Kaizu K, Tamura S, Nozaki T, Kokubo T, Takahashi K (2015) The

physical size of transcription factors is key to transcriptional regulation in chromatin domains. *J Phys Condens Matter* **27**(6)**:** 064116

Maeshima K, Yahata K, Sasaki Y, Nakatomi R, Tachibana T, Hashikawa T, Imamoto F, Imamoto N (2006) Cell-cycle-dependent dynamics of nuclear pores: pore-free islands and lamins. *J Cell Sci* **119**(Pt 21)**:** 4442-4451

Magistrato A, Ruggerone P, Spiegel K, Carloni P, Reedijk J (2006) Binding of novel azole-bridged dinuclear platinum(II) anticancer drugs to DNA: insights from hybrid QM/MM molecular dynamics simulations. *J Phys Chem B* **110**(8)**:** 3604-3613

Mah LJ, El-Osta A, Karagiannis TC (2010) GammaH2AX as a molecular marker of aging and disease. *Epigenetics* **5**(2)**:** 129-136

Maison C, Almouzni G (2004) HP1 and the dynamics of heterochromatin maintenance. *Nat Rev Mol Cell Biol* **5**(4)**:** 296-304

Maison C, Quivy JP, Probst AV, Almouzni G (2010) Heterochromatin at mouse pericentromeres: a model for de novo heterochromatin formation and duplication during replication. *Cold Spring Harb Symp Quant Biol* **75:** 155-165

Malina J, Kasparkova J, Farrell NP, Brabec V (2011) Walking of antitumor bifunctional trinuclear PtII complex on double-helical DNA. *Nucleic Acids Res* **39**(2)**:** 720-728

Mansy S, Rosenberg B, Thomson AJ (1973) Binding of cis- and trans-dichlorodiammineplatinum(II) to nucleosides. I. Location of the binding sites. *J Am Chem Soc* **95**(5)**:** 1633-1640

Marenduzzo D, Finan K, Cook PR (2006) The depletion attraction: an underappreciated force driving cellular organization. *J Cell Biol* **175**(5)**:** 681-686

Markaki Y, Gunkel M, Schermelleh L, Beichmanis S, Neumann J, Heidemann M, Leonhardt H, Eick D, Cremer C, Cremer T (2010) Functional nuclear organization of transcription and DNA replication: a topographical marriage between chromatin domains and the interchromatin compartment. *Cold Spring Harb Symp Quant Biol* **75:** 475-492

Matsuyama S, Shimura M, Fujii M, Maeshima K, Yumoto H, Mimura H, Sano Y, Yabashi M, Nishino Y, Tamasaku K, Ishizaka Y, Ishikawa T, Yamauchi K (2010) Elemental mapping of frozen hydrated cells with cryo-scanning X-ray fluorescence microscopy. *X-Ray Spectrometry* **39:** 260-266

Metropolis N, Rosenbluth AW, M.N. R, Teller AH, Teller E (1953) Equation of State Calculations by Fast Computing Machines *J Chem Phys* **21**(6)**:** 1087 (1086 pages)

Mlcouskova J, Kasparkova J, Suchankova T, Komeda S, Brabec V (2012a) DNA conformation and repair of polymeric natural DNA damaged by antitumor azolato-bridged dinuclear Pt(II) complex. *J Inorg Biochem* **114:** 15-23

Mlcouskova J, Malina J, Novohradsky V, Kasparkova J, Komeda S, Brabec V (2012b) Energetics, conformation, and recognition of DNA duplexes containing a major adduct of an anticancer azolato-bridged dinuclear Pt(II) complex. *Biochim Biophys Acta* **1820**(10)**:** 1502-1511

Morelli MJ, ten Wolde PR (2008) Reaction Brownian dynamics and the effect of spatial fluctuations on the gain of a push-pull network. *J Chem Phys* **129**(5)**:** 054112

Morris SJ (1990) Real-time multi-wavelength fluorescence imaging of living cells. *Biotechniques* **8**(3)**:** 296-308

Nakajima T, Sado T (2014) Current view of the potential roles of proteins enriched on the inactive X chromosome. *Genes Genet Syst* **89**(4)**:** 151-157

Nan X, Tate P, Li E, Bird A (1996) DNA methylation specifies chromosomal localization of MeCP2. *Mol Cell Biol* **16**(1)**:** 414-421

Niedojadlo J, Perret-Vivancos C, Kalland KH, Cmarko D, Cremer T, van Driel R, Fakan S (2011) Transcribed DNA is preferentially located in the perichromatin region of mammalian cell nuclei. *Exp Cell Res* **317**(4)**:** 433-444

Nora EP, Lajoie BR, Schulz EG, Giorgetti L, Okamoto I, Servant N, Piolot T, van Berlum NL, Meisig J, Sedat JW, Gribnau J, Barillot E, BLüthgen N, Dekker J, Heard E

(2012) Spatial partitioning of the regulatory landscape of the X-inactivation centre. *Nature* **485**(7398)**:** 381-385.

Nozaki T, Imai R, Tanbo M, Nagashima R, Tamura S, Tani T, Joti Y, Tomita M, Hibino K, Kanemaki MT, Wendt KS, Okada Y, Nagai T, Maeshima K (2017) Dynamic Organization of Chromatin Domains Revealed by Super-Resolution Live-Cell Imaging. *Mol Cell* **67**(2)**:** 282-293 e287

Nozaki T, Kaizu K, Pack CG, Tamura S, Tani T, Hihara S, Nagai T, Takahashi K, Maeshima K (2013) Flexible and dynamic nucleosome fiber in living mammalian cells. *Nucleus* **4**(5)**:** 349-356

Nozawa RS, Nagao K, Igami KT, Shibata S, Shirai N, Nozaki N, Sado T, Kimura H, Obuse C (2013) Human inactive X chromosome is compacted through a PRC2-independent SMCHD1-HBiX1 pathway. *Nat Struct Mol Biol* **20**(5)**:** 566-573

Ochs RL, Lischwe MA, Spohn WH, Busch H (1985) Fibrillarin: a new protein of the nucleolus identified by autoimmune sera. *Biol Cell* **54**(2)**:** 123-133

Oldenbourg RaS, M (2010) Microscopes. In *Handbook of Optics*, Michael Bass JME, Vasudevan Lakshminarayanan, Guifang Li, Carolyn Macdonald, Virendra N. Mahajan, Eric Van Stryland (ed), 3rd edn, pp 28.21 – 28.62. New York: McGraw-Hill, Inc

Ou HD, Phan S, Deerinck TJ, Thor A, Ellisman MH, O'Shea CC (2017) ChromEMT: Visualizing 3D chromatin structure and compaction in interphase and mitotic cells. *Science* **357**(6349): eaag0025

Ozer G, Luque A, Schlick T (2015) The chromatin fiber: multiscale problems and approaches. *Current opinion in structural biology* **31:** 124-139

Park GY, Wilson JJ, Song Y, Lippard SJ (2012) Phenanthriplatin, a monofunctional DNA-binding platinum anticancer drug candidate with unusual potency and cellular activity profile. *Proc Natl Acad Sci U S A* **109**(30)**:** 11987-11992

Peterson EJ, Menon VR, Gatti L, Kipping R, Dewasinghe D, Perego P, Povirk LF, Farrell NP (2015) Nucleolar targeting by platinum: p53-independent apoptosis follows

rRNA inhibition, cell-cycle arrest, and DNA compaction. *Mol Pharm* **12**(1)**:** 287-297

Pickard AJ, Liu F, Bartenstein TF, Haines LG, Levine KE, Kucera GL, Bierbach U (2014) Redesigning the DNA-targeted chromophore in platinum-acridine anticancer agents: a structure-activity relationship study. *Chemistry* **20**(49)**:** 16174-16187

Pliss A, Kuzmin AN, Kachynski AV, Prasad PN (2010) Nonlinear optical imaging and Raman microspectrometry of the cell nucleus throughout the cell cycle. *Biophys J* **99**(10)**:** 3483-3491

Pollard TD, Earnshaw WC, Lippincott-Schwartz J, Johnson G (2016) Cell Biology, 3rd Edition.

Rao SS, Huntley MH, Durand NC, Stamenova EK, Bochkov ID, Robinson JT, Sanborn AL, Machol I, Omer AD, Lander ES, Aiden EL (2014) A 3D map of the human genome at kilobase resolution reveals principles of chromatin looping. *Cell* **159**(7)**:** 1665-1680

Ricci MA, Manzo C, Garcia-Parajo MF, Lakadamyali M, Cosma MP (2015) Chromatin fibers are formed by heterogeneous groups of nucleosomes in vivo. *Cell* **160**(6)**:** 1145-1158

Rixe O, Ortuzar W, Alvarez M, Parker R, Reed E, Paull K, Fojo T (1996) Oxaliplatin, tetraplatin, cisplatin, and carboplatin: spectrum of activity in drug-resistant cell lines and in the cell lines of the National Cancer Institute's Anticancer Drug Screen panel. *Biochem Pharmacol* **52**(12)**:** 1855-1865

Rogakou EP, Pilch DR, Orr AH, Ivanova VS, Bonner WM (1998) DNA double-stranded breaks induce histone H2AX phosphorylation on serine 139. *J Biol Chem* **273**(10)**:** 5858-5868

Rosenberg B, VanCamp L (1970) The successful regression of large solid sarcoma 180 tumors by platinum compounds. *Cancer Res* **30**(6)**:** 1799-1802

Sakai W, Swisher EM, Karlan BY, Agarwal MK, Higgins J, Friedman C, Villegas E, Jacquemont C, Farrugia DJ, Couch FJ, Urban N, Taniguchi T (2008) Secondary mutations as a mechanism of cisplatin resistance in BRCA2-mutated cancers. *Nature*

451(7182)**:** 1116-1120

Saksouk N, Simboeck E, Dejardin J (2015) Constitutive heterochromatin formation and transcription in mammals. *Epigenetics Chromatin* **8**(3)**:** 3

Sanborn AL, Rao SS, Huang SC, Durand NC, Huntley MH, Jewett AI, Bochkov ID, Chinnappan D, Cutkosky A, Li J, Geeting KP, Gnirke A, Melnikov A, McKenna D, Stamenova EK, Lander ES, Aiden EL (2015) Chromatin extrusion explains key features of loop and domain formation in wild-type and engineered genomes. *Proc Natl Acad Sci U S A* **112**(47)**:** E6456-6465

Schneider CA, Rasband WS, Eliceiri KW (2012) NIH Image to ImageJ: 25 years of image analysis. *Nat Methods* **9**(7)**:** 671-675

Schwarz PM, Hansen JC (1994) Formation and stability of higher order chromatin structures. Contributions of the histone octamer. *J Biol Chem* **269**(23)**:** 16284-16289

Scott MS, Boisvert FM, McDowall MD, Lamond AI, Barton GJ (2010) Characterization and prediction of protein nucleolar localization sequences. *Nucleic Acids Res* **38**(21)**:** 7388-7399

Sexton T, Yaffe E, Kenigsberg E, Bantignies F, Leblanc B, Hoichman M, Parrinello H, Tanay A, Cavalli G (2012) Three-Dimensional Folding and Functional Organization Principles of the Drosophila Genome. *Cell* **148**(3)**:** 458-472

Shimura M, Saito A, Matsuyama S, Sakuma T, Terui Y, Ueno K, Yumoto H, Yamauchi K, Yamamura K, Mimura H, Sano Y, Yabashi M, Tamasaku K, Nishio K, Nishino Y, Endo K, Hatake K, Mori Y, Ishizaka Y, Ishikawa T (2005) Element array by scanning X-ray fluorescence microscopy after cis-diamminedichloro-platinum(II) treatment. *Cancer Res* **65**(12)**:** 4998-5002

Shinkai S, Nozaki T, Maeshima K, Togashi Y (2016) Dynamic nucleosome movement tells Structural information of topological chromatin domains in human cells. *PLoS Computational Biology* **12**(10)**:** e1005136

Shribak M (2013) Quantitative orientation-independent differential interference contrast

microscope with fast switching shear direction and bias modulation. *J Opt Soc Am A Opt Image Sci Vis* **30**(4)**:** 769-782

Shribak M (2014) Compact Orientation-Independent Differential Interference Contrast (OI-DIC) Microscope Designed for High Resolution and High Sensitivity Mapping of Optical Path and Optical Path Gradient. *Microsc Microanal* **20**(Suppl 3)**:** 1350-1351

Shribak M, Inoue S (2006) Orientation-independent differential interference contrast microscopy. *Appl Opt* **45**(3)**:** 460-469

Shribak M, Larkin KG, Biggs D (2017) Mapping optical path length and image enhancement using quantitative orientation-independent differential interference contrast microscopy. *J Biomed Opt* **22**(1)**:** 16006

Smeets D, Markaki Y, Schmid VJ, Kraus F, Tattermusch A, Cerase A, Sterr M, Fiedler S, Demmerle J, Popken J, Leonhardt H, Brockdorff N, Cremer T, Schermelleh L, Cremer M (2014) Three-dimensional super-resolution microscopy of the inactive X chromosome territory reveals a collapse of its active nuclear compartment harboring distinct Xist RNA foci. *Epigenetics Chromatin* **7**(8)**:** 8

Stordal B, Pavlakis N, Davey R (2007) Oxaliplatin for the treatment of cisplatin-resistant cancer: a systematic review. *Cancer Treat Rev* **33**(4)**:** 347-357

Takata H, Hanafusa T, Mori T, Shimura M, Iida Y, Ishikawa K, Yoshikawa K, Yoshikawa Y, Maeshima K (2013) Chromatin compaction protects genomic DNA from radiation damage. *PLoS One* **8**(10)**:** e75622

Teletchea S, Komeda S, Teuben JM, Elizondo-Riojas MA, Reedijk J, Kozelka J (2006) A pyrazolato-bridged dinuclear platinum(II) complex induces only minor distortions upon DNA-binding. *Chemistry* **12**(14)**:** 3741-3753

Todd RC, Lippard SJ (2009) Inhibition of transcription by platinum antitumor compounds. *Metallomics* **1**(4)**:** 280-291

Tokunaga M, Imamoto N, Sakata-Sogawa K (2008) Highly inclined thin illumination enables clear single-molecule imaging in cells. *Nat Methods* **5**(2)**:** 159-161

Toth KF, Knoch TA, Wachsmuth M, Frank-Stohr M, Stohr M, Bacher CP, Muller G, Rippe K (2004) Trichostatin A-induced histone acetylation causes decondensation of interphase chromatin. *J Cell Sci* **117**(Pt 18)**:** 4277-4287

Trojer P, Reinberg D (2007) Facultative heterochromatin: is there a distinctive molecular signature? *Mol Cell* **28**(1)**:** 1-13

Uemura M, Hoshiyama M, Furukawa A, Sato T, Higuchi Y, Komeda S (2015) Highly efficient uptake into cisplatin-resistant cells and the isomerization upon coordinative DNA binding of anticancer tetrazolato-bridged dinuclear platinum(ii) complexes. *Metallomics* **2015:** 22

Uemura M, Suzuki T, Nishio K, Chikuma M, Komeda S (2012) An in vivo highly antitumor-active tetrazolato-bridged dinuclear platinum(II) complex largely circumvents in vitro cisplatin resistance: two linkage isomers yield the same product upon reaction with 9-ethylguanine but exhibit different cytotoxic profiles. *Metallomics* **4**(7)**:** 686-692

Van Holde KE, Weischet WO (1978) Boundary analysis of sedimentation-velocity experiments with monodisperse and paucidisperse solutes. *Biopolymers* **17**(6)**:** 1387-1403

Walter A, Chapuis C, Huet S, Ellenberg J (2013) Crowded chromatin is not sufficient for heterochromatin formation and not required for its maintenance. *J Struct Biol* **184**(3)**:** 445-453

Wang S, Su JH, Beliveau BJ, Bintu B, Moffitt JR, Wu CT, Zhuang X (2016) Spatial organization of chromatin domains and compartments in single chromosomes. *Science* **353**(6299)**:** 598-602

Watson JD, Baker TA, Bell SP, Gann A, Levine M, Losick R (2013) Molecular Biology of the Gene, 7/E.

Wu R, Singh PB, Gilbert DM (2006) Uncoupling global and fine-tuning replication timing determinants for mouse pericentric heterochromatin. *J Cell Biol* **174**(2)**:** 185-194

Wutz A (2011) Gene silencing in X-chromosome inactivation: advances in understanding facultative heterochromatin formation. *Nat Rev Genet* **12**(8)**:** 542-553

Yamamoto K, Hirano S, Ishiai M, Morishima K, Kitao H, Namikoshi K, Kimura M, Matsushita N, Arakawa H, Buerstedde JM, Komatsu K, Thompson LH, Takata M (2005) Fanconi anemia protein FANCD2 promotes immunoglobulin gene conversion and DNA repair through a mechanism related to homologous recombination. *Mol Cell Biol* **25**(1)**:** 34-43

Yamauchi K, Yamamura K, Mimura H, Sano Y, Saito A, Endo K, Souvorov A, Yabashi M, Tamasaku K, Ishikawa T, Mori Y (2003) Two-dimensional Submicron Focusing of Hard X-rays by Two Elliptical Mirrors Fabricated by Plasma Chemical Vaporization Machining and Elastic Emission Machining. *Japanese journal of applied physics Pt 1, Regular papers & short notes* **42**(11)**:** 7129-7134

Yoshikawa Y, Komeda S, Uemura M, Kanbe T, Chikuma M, Yoshikawa K, Imanaka T (2011) Highly efficient DNA compaction mediated by an in vivo antitumor-active tetrazolato-bridged dinuclear platinum(II) complex. *Inorg Chem* **50**(22)**:** 11729-11735

Yuan SS, Lee SY, Chen G, Song M, Tomlinson GE, Lee EY (1999) BRCA2 is required for ionizing radiation-induced assembly of Rad51 complex in vivo. *Cancer Res* **59**(15)**:** 3547-3551

Zimmer C, Wähnert U (1986) Nonintercalating DNA-binding ligands: Specificity of the interaction and their use as tools in biophysical, biochemical and biological investigations of the genetic material. *Progress in Biophysics and Molecular Biology* **47**(1)**:** 31-112